Document Version
Final published version

Licence
CC BY

JGR Solid Earth

Key Points:

- We develop a new semi-analytical approach to predict fluid pressure in a borehole embedded in poroelastic media for an incident plane P wave
- We derive analytical solutions and verify them against finite-difference Biot-poroelasticity simulations
- We quantify tube-wave generation from elastic contrasts, porous flow, and borehole-radius changes to aid borehole data interpretation

Correspondence to:
S. Minato,
s.minato@aist.go.jp

A Semi-Analytical Approach to Model Borehole Tube Waves for Interpretation of Downhole Seismic Data in Fault Zones

Shohei Minato[1,2] , Ranajit Ghose[2] , and Tsutomu Kiguchi[1]

[1]Geological Survey of Japan, National Institute of Advanced Industrial Science and Technology (AIST), Tsukuba, Japan, [2]Department of Geoscience and Engineering, Delft University of Technology, Delft, The Netherlands

Abstract Understanding fault-zone permeability is crucial in model-based assessment of fluid migration, earthquake nucleation, and hydrothermal or hydrocarbon systems. Vertical seismic profiling (VSP) often captures Stoneley (tube) waves generated by fluid-formation coupling in and around a borehole. Tube waves offer valuable constrains to local hydraulic properties. Full simulation of the generation of tube waves using Biot's poroelastic equations is very important, but computationally demanding due to the multiscale nature of the problem, involving fine-scale borehole geometry and long-wavelength seismic wave propagation in the layered media. We develop a semi-analytical approach that can predict borehole pressure response of a normally incident plane P wave in layered poroelastic media, including irregularities in the borehole radius. The model accounts for three key mechanisms for tube-wave generation: (a) due to elastic impedance contrasts, (b) due to fluid infiltration from poroelastic layers, and (c) due to borehole-radius changes. Using a propagator-matrix formulation under low-frequency assumptions, we derive closed-form expressions for the tube-wave amplitudes and validate them using finite-difference poroelastic simulations. The results show that elastic boundaries produce tube waves with opposite polarities, while a thin porous layer and a thin elastic layer generate asymmetric responses with notably different frequency spectra. Our approach improves upon previous effective-source models by accounting for the tube-wave velocity contrasts and ensuring the consistency with the poroelastic theory. This efficient modeling framework enables clearer interpretation of VSP data in fault zones, providing insights that aid in quantitative estimation of the local hydraulic properties.

Plain Language Summary Underground rock formations, especially in fault zones, can store and move fluids in ways that affect the occurrence of earthquakes and the extraction of subsurface energy resources. Understanding how easily a fluid flows through these rocks, known as permeability, is vital to earthquake science, geothermal energy, and groundwater management. One established approach to investigate permeability uses seismic waves recorded in water-filled borehole, where characteristic signals called tube waves are sensitive to the surrounding rock and fluid properties. In this research, we develop a new and efficient modeling framework to better understand how tube waves are generated when seismic waves interact with a borehole. Our method uses a simplified mathematical model to calculate how different factors contribute to the tube-wave signals. We study how three main causes—changes in the rock layers, fluid movement in the porous zones, and irregular borehole shapes—affect the tube-wave characteristics. Although the computation is extremely fast, the derived results match closely with those obtained through very complex and computationally expensive simulations. The new approach enables more efficient analysis of the field data and improved capacity to monitor underground fluid pathways, especially in active fault zones.

1. Introduction

Hydraulic properties of a fault zone, especially the spatial heterogeneity, stress dependence, and temporal changes of permeability, are key to understanding the fluid circulation in fractured media and the deformation processes in the upper crust. Fault zones often act as complex conduit-barrier systems, where permeability structure governs fluid migration, trapping, and overpressure of fluids, with critical implications for earthquake nucleation and rupture propagation (e.g., Uehara & Shimamoto, 2004; Wibberley et al., 2008). The permeability architecture of fault zones also influences ground water flow, hydrocarbon migration, and hydrothermal fluid circulation in geothermal systems (e.g., Bense et al., 2013). Therefore, a detailed knowledge of the distribution and evolution of fault zone permeability is essential not only for understanding earthquake mechanisms and assessing seismic hazards, but also for optimizing strategies in groundwater management and exploration of hydrocarbon and geothermal resources.

Borehole measurements provide in situ estimates of hydraulic properties under realistic stress and heterogeneity conditions, without disturbances associated with sample collection and laboratory preparation. Among the various measurement approaches, the observation of acoustic waves in a fluid-filled borehole (e.g., Beydoun et al., 1985; Tang & Cheng, 1996) leads to a direct method to induce and measure fluid flow under in situ conditions. Complementary to packer tests, which isolate specific depth intervals (e.g., Cook, 2003), acoustic measurements in boreholes efficiently provide hydraulic information at multiple depths despite their limited penetration range (typically 5–6 times the borehole radius at 2 kHz; Sinha & Asvadurov, 2004). Because the borehole fluid communicates directly with the formation's pore fluid at the borehole wall, the permeability effects can be captured from the observed interaction of the acoustic waves. This wavefield includes the Biot slow wave resulting from dynamic poroelasticity (Biot, 1956a, 1956b, 1962), which behaves diffusively at the low frequencies following Darcy's law and propagates at higher frequencies under the control of tortuosity (Johnson et al., 1987). A clear understanding of these dynamic interactions is, therefore, crucial for interpreting borehole acoustic data and accurately estimating in situ hydraulic properties.

Research on dynamic interaction between the borehole fluid and the surrounding formations has so far focused extensively on full-waveform acoustic logging using Stoneley (tube) waves (e.g., Biot, 1952; Cheng et al., 1987; Chang et al., 1988; Fan & Smeulders, 2013; Sidler et al., 2014, among many others). The Stoneley wave is an axially symmetric fundamental-mode interface wave that propagates along the borehole and, unlike other guided modes, does not have a cut-off frequency and exists at all frequencies (White, 1983). At low frequencies where the seismic wavelength is much larger than the borehole radius, it behaves as a piston-like compression of the borehole fluid, commonly referred to as a tube wave (Endo, 2006), and dominates the low-frequency portion of the data (Tang & Cheng, 1993). To orient the reader, Figure 1 illustrates the two acquisition geometries considered in this study: full-waveform sonic logging with a downhole source and many receivers, and vertical seismic profiling (VSP) with a surface source and downhole receivers at many depths. The figure also shows examples of the recorded data. In both cases, tube waves generated or reflected at a heterogeneity propagate upward and downward along the borehole fluid column. In acoustic logging, although monopole transmitters often operate at higher center frequencies for body-wave measurements (typically on the order of 5–10 kHz), the tube-wave energy relevant to permeability-effects is concentrated at lower frequencies. Many commercial tools, therefore, provide a dedicated low-frequency monopole "Stoneley mode" (commonly ∼0.5–1 kHz) to deliberately excite and record tube waves. Analyses of tube-wave attenuation, dispersion, and reflection have long been employed to estimate hydraulic permeability (e.g., Endo, 2006; Tang & Cheng, 1993, 1996; Tang et al., 1991). The high sensitivity of tube waves to formation permeability has proven to be useful for monitoring the boreholes and their surrounding, during fluid production (Bakulin et al., 2008).

While acoustic logging operates in the kilohertz range, VSP typically measures lower-frequency waves (up to a few hundred hertz) using a surface seismic source. Though often aimed at estimating the seismic velocity structure around a borehole, VSP can capture the tube waves generated by interactions between borehole fluid and porous formations, particularly when hydrophones are used in an open borehole, where the borehole fluid is hydraulically connected to the surrounding formation. To clarify the geometry and the processes involved (Figure 1c), a typical VSP survey places a seismic source at or near the Earth's surface and deploys an array of receivers at various depths in the borehole. The recorded wavefield generally includes: (a) a downgoing P wave traveling directly from the source to the downhole receivers; (b) an upgoing reflected P wave from the subsurface interfaces; and (c) tube waves propagating along the borehole fluid column when the body waves interact with the fractures or other discrete interfaces. Although tube waves in a VSP have generally been considered as noise (e.g., Hardage, 1981), several studies have exploited their large amplitudes to infer permeability (Beydoun et al., 1985; Hardin et al., 1987; Huang & Hunter, 1984; Kiguchi et al., 2001; Li et al., 1994). Hydrophone-based VSP has also been recommended for many years in order to achieve a significant reduction in the data-acquisition cost (e.g., Greenwood et al., 2012; Marzetta et al., 1988; Milligan et al., 1997). More recently, Greenwood et al. (2019) have shown that tube waves observed using a slotted PVC casing are similar to those detected using an open hole, suggesting the feasibility of permeability monitoring without long-term maintenance of an open borehole.

Compared to acoustic logging, the lower frequency range used in VSP results in greater effective fluid mobility near the borehole wall, leading to a larger oscillatory fluid flux for a given pore-pressure gradient (Tang et al., 1991). Moreover, the downgoing body-wave field in VSP can convert efficiently to tube waves at permeable layers, causing a local increase in tube-wave energy. In contrast, in acoustic logging, the total tube-
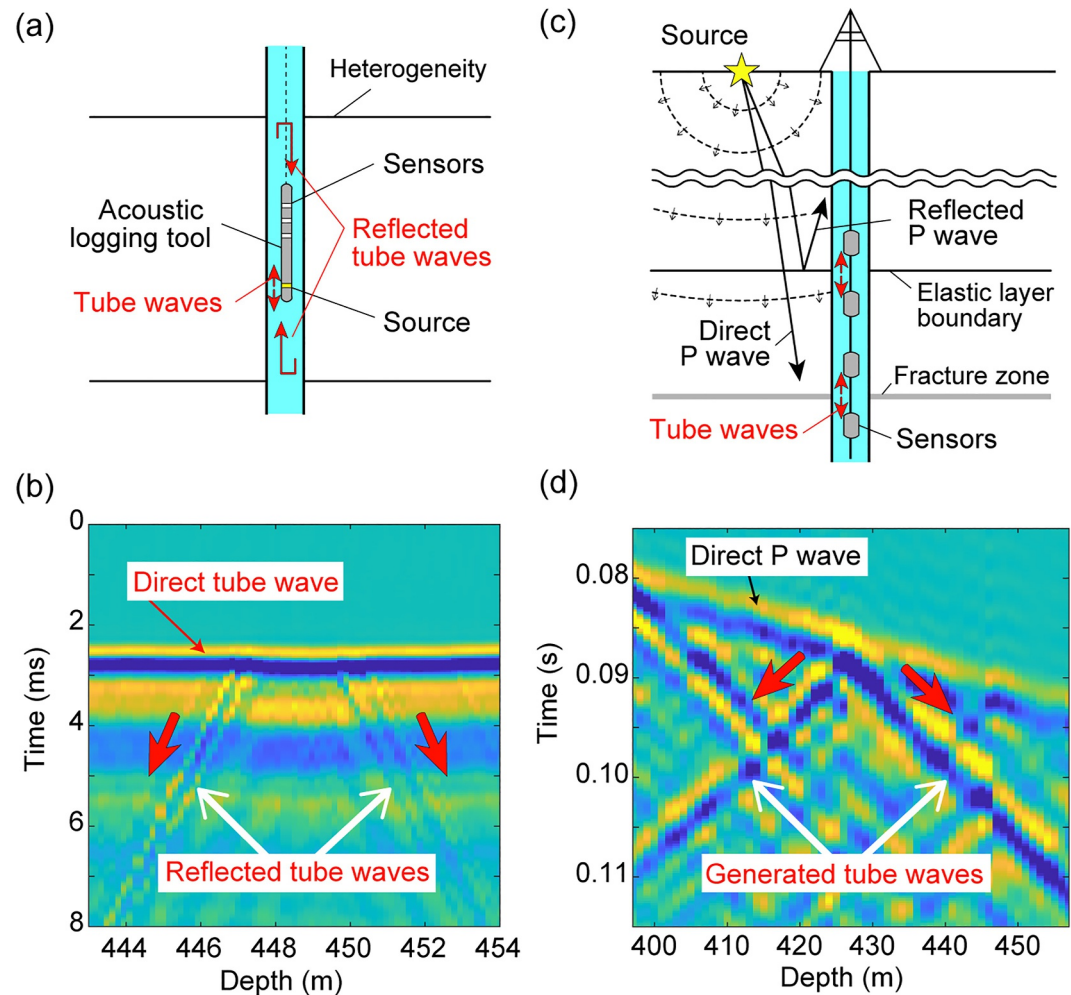
Figure 1. Schematic and data examples of the tube (Stoneley) waves in two acquisition geometries. (a) Acoustic logging (downhole source and receivers). A low-frequency monopole source at a certain tool depth excites the tube waves. The tube wave is reflected at a depth where it encounters a change in the medium (heterogeneity). The upgoing and downgoing tube waves traveling along the borehole fluid column are generated. (b) An example of acoustic logging data (Stoneley mode) showing the waveform of the near-offset receiver at each tool depth. Arrows mark the direct tube wave and the reflected tube waves. The frequency spectrum peaks near ∼0.5 kHz but retains appreciable energy over a broader band (a few 10^2 Hz to ∼3 kHz). Traces are RMS-amplitude-normalized and band-passed for display. (c) Schematic illustration of vertical seismic profiling (VSP) data (surface source, downhole receivers). The wavefield includes downgoing P waves, reflected upgoing P waves, and tube waves propagating along the borehole fluid. Tube waves are generated by interactions between borehole fluid and heterogeneities in the surrounding porous formation. (d) Hydrophone VSP data showing tube-wave conversions from P wave and their upward and downward propagation along the borehole.

wave energy generally diminishes due to pressure diffusion into the formation. These two factors suggest that hydrophone-based VSP may offer increased sensitivity to hydraulically active zones, while also benefiting from efficient depth coverage through simultaneous wavefield recordings at multiple depths using a downhole receiver array.

VSP measurements differ from acoustic logging primarily in how the incident waves excite the tube waves. In VSP, elastic body waves from a surface seismic source travel through the subsurface and interact with the borehole (Figure 1c). Previous studies have identified three main mechanisms through which the incident P wave can generate tube waves in a VSP:

1. Fluid infiltration from a porous layer or open fractures (Figure 2a), where an incident P wave compresses the permeable formation and drives fluid into the borehole (e.g., Bakku et al., 2013; Beydoun et al., 1985; Hardin
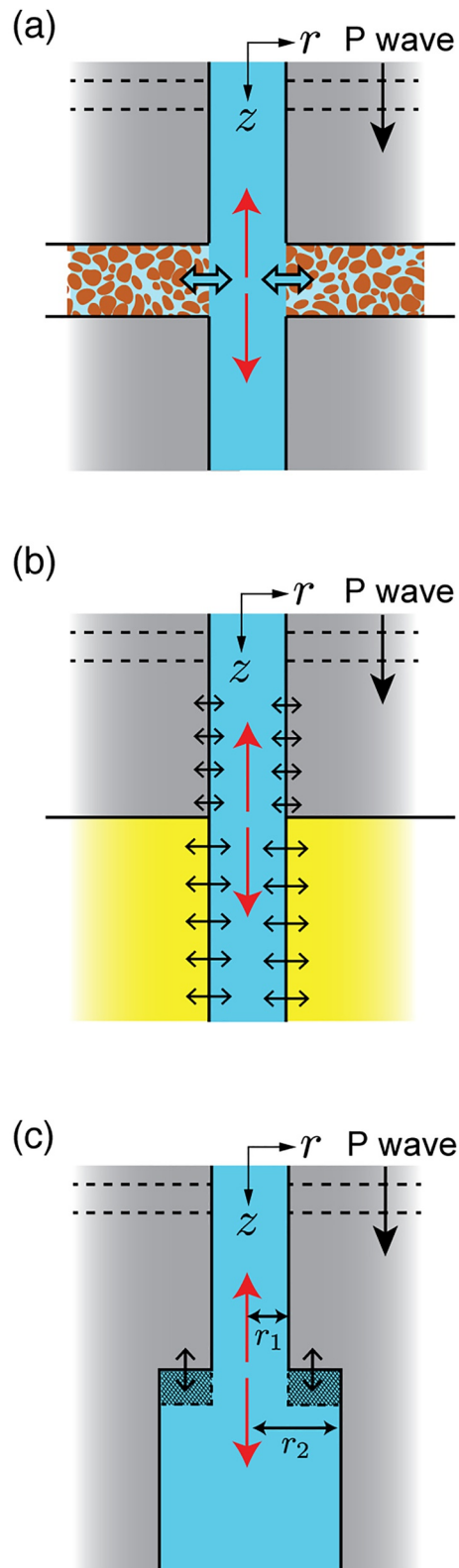
Figure 2.

et al., 1987; Ionov, 2007; Li et al., 1994; Minato, Ghose, Kiguchi, & Tsuji, 2017; Minato, Ghose, Tsuji, et al., 2017).

2. Borehole squeezed by elastic-wave-induced radial strain (Figure 2b), which produces fluid pressure changes when a passing P wave deforms the borehole wall (Kurkjian et al., 1994; Peng et al., 1996).

3. Borehole-radius discontinuities (Figure 2c), where a step-like change in the borehole radius (r) acts as a piston, producing tube waves when impinged by an external wave disturbance (Hardage, 1981; White & Lessenger, 1988).

Although these mechanisms can each generate tube waves, their relative contributions remain poorly quantified on field data, especially at a fault zone where multiple mechanisms may be active simultaneously. Previous studies have reported correlation between tube-wave generation depths and subsurface properties, e.g., fractures, impedance boundaries, or borehole irregularities (e.g., Beydoun et al., 1985; Evans et al., 2005; Greenwood et al., 2019; Kiguchi et al., 2001; Li et al., 1994). However, such correlations alone do not provide quantitative interpretation. For example, Figure 3a shows hydrophone VSP data from an active fault zone in Japan (Kiguchi et al., 2001). These data clearly illustrate tube waves generated at discrete depths in response to an incident P wave, which is a pattern consistent with prior observations. While some of these depths correlate well with the location of the permeable structures (Kiguchi et al., 2001), substantial variations in logged P- and S-wave velocities (measured at sonic frequencies), as well as in density, borehole radius, and porosity (Figure 3b) suggest that multiple factors possibly influence tube-wave generation at each interface.

A rigorous forward-modeling approach that solves the Biot's dynamic poroelastic equations in three-dimensions could, in principle, capture all three generation mechanisms. However, such simulations, often using finite-difference (FD) or finite-element methods, are computationally expensive due to the multiscale nature of wave propagation (centimeter-scale borehole radius, decameter-scale wavelengths, and propagation distances of hundreds of meters). Moreover, because they produce complete wavefields, the tube-wave signals must be identified and extracted, which makes it difficult to directly relate their amplitudes to specific material or geometric parameters without substantial post-processing.

In this study, we present a more efficient semi-analytical framework that accounts for all three primary tube-wave generation mechanisms in a layered poroelastic medium and in the presence of borehole irregularities (Figure 2). Building upon the borehole coupling theory (e.g., Ionov & Maximov, 1996; Peng et al., 1996), we go further to incorporate borehole-radius changes and ensure low-frequency consistency with Biot's poroelasticity for porous layers.

We simplify the problem by separating it into two subproblems: (a) elastic wave propagation in layered media without a borehole, and (b) fluid-pressure changes in a cylindrical borehole under a quasi-static/low-frequency

Figure 2. Illustration of three different mechanisms that can generate tube waves (red arrows) in a fluid-filled borehole due to an incident P wave. The cylindrical coordinate system (r−z) is considered. (a) Fluid infiltration (blue arrows) from the porous formation. (b) The difference in the degree of radial strain (black horizontal arrows) at the borehole wall when an elastic-layer boundary is encountered. (c) The local change of fluid volume (hatched area) at a borehole irregularity (e.g., a step-like change in the borehole radius).

assumption where the seismic wavelength is much larger than the borehole radius. For a normally incident plane P wave, the system of equations is solved using the propagator matrix method (Aki & Richards, 2002), yielding waveforms including elastic waves and tube waves. This formulation also provides closed-form expressions for tube-wave amplitudes, explicitly relating them to layer properties and borehole geometry. As a result, our framework can efficiently estimate downhole-observed waveforms and tube-wave amplitudes, while distinguishing the contribution of each tube-wave generation mechanism.

In Section 2, we present the governing equations and develop the propagator-matrix formulation for layered formations. Section 3 derives closed-form expressions for tube-wave amplitudes associated with the three mechanisms: (a) an elastic contrast at a layer boundary (Figure 2b), (b) a porous layer embedded between elastic layers (Figure 2a), and (c) a step-like change in borehole radius (Figure 2c). In Section 4, the semi-analytical solutions are validated against finite-difference (FD) simulations that explicitly model the wave propagation in poroelastic media. Finally, Section 5 compares our results with earlier solutions and discusses their broader implications.

2. A Semi-Analytical Modeling Approach

In this section, we present a simplified, semi-analytical approach for computing tube-wave responses. Section 2.1 presents the low-frequency theory for borehole–formation interaction and introduces a revised boundary condition to ensure consistency with the Biot poroelasticity. Section 2.2 reformulates the problem using the propagator matrix method and generalized source terms, enabling efficient calculation of the full waveforms and closed-form expressions for the tube-wave amplitudes.

2.1. Governing Equation With a Revised Boundary Condition

The low-frequency behavior of the tube waves in fluid-filled boreholes has long been studied in terms of coupling between the borehole fluid and the surrounding elastic solid. White (1953, 1983) analyzed the tube waves in fluid-filled boreholes, including their phase velocity and sensitivity to formation properties, and showed how incident elastic waves couple with the fluid pressure in the borehole. Extending these concepts, Ionov and Maximov (1996) formulated a quasi-static poroelastic theory that models tube-wave generation due to external elastic waves. In this study, we further advance the model by (a) revising the pore-pressure boundary condition far from the borehole to ensure consistency with the Biot's dynamic poroelasticity in the long-wavelength limit, and (b) introducing a new source mechanism for borehole-radius irregularities. We summarize below the governing system that forms the basis for the propagator matrix method (Section 2.2).

2.1.1. Governing System

We consider the small-amplitude wave motion in a fluid-filled circular cylinder embedded in poroelastic media (e.g., an open borehole). Under the long-wavelength approximation, the borehole fluid is treated as a one-dimensional acoustic medium in which the state variables p and v_z depend only on z and ω (White, 1983). With this assumption, the governing system for (p, v_z) can be written as

$$\frac{\partial}{\partial z}\begin{pmatrix} p \\ v_z \end{pmatrix} = i\omega \begin{pmatrix} 0 & \rho_f \\ K_f^{-1} & 0 \end{pmatrix}\begin{pmatrix} p \\ v_z \end{pmatrix} + \begin{pmatrix} 0 \\ -\dfrac{2}{R} v_r|_{r=R} \end{pmatrix}, \tag{1}$$

where ρ_f is the fluid density and K_f the fluid bulk modulus. The last term represents the radial fluid velocity at the borehole wall, $v_r(r, z, \omega)_{r=R}$. If this term is neglected, the system reduces to the one-dimensional acoustic relation for water with bulk modulus K_f. Retaining v_r allows borehole–formation coupling such as wall compliance and fluid infiltration to be incorporated into the system.

2.1.2. Radial Fluid Motion at the Wall

We decompose v_r in Equation 1 into three contributions (Ionov & Maximov, 1996):

$$v_r|_{r=R} = -\frac{i\omega R}{2\mu}p - \frac{i\omega R}{E}\sigma_{\text{eff}}^{\text{ext}} + v_{\text{ft}}, \tag{2}$$

where μ and E are the shear and Young's moduli of the surrounding medium. The first term is the intrinsic wall compliance driven by borehole pressure (White, 1983); it is present regardless of external waves or permeability. The second term is the deformation forced by the external elastic field (Figure 2b); it vanishes when no elastic waves are present. The third term accounts for the fluid infiltration from a permeable formation (Figure 2a); it persists even without external waves and disappears in the impermeable limit.

The governing system is expressed in terms of (p, v_z). The first and third contributions on the right-hand side of Equation 2 depend on p. The second contribution, however, is prescribed from the elastic wavefield (subproblem 1), which is treated separately from the borehole-fluid problem (subproblem 2). The effect of borehole irregularities (Figure 2c) is not contained in v_r and will be introduced separately as a local volume-injection source in the propagator-matrix formulation.

2.1.2.1. Deformation Due To Externally Propagating Elastic Waves

For a normally incident plane P wave with displacement potential $\phi_E(z) = D_E \exp(ik_p z) + U_E \exp(-ik_p z)$, where $k_p = \omega/V_P$ (see also Appendix A), the effective external stress in Equation 2 is given by (e.g., Ionov & Maximov, 1996):

$$\sigma_{\text{eff}}^{\text{ext}}(z) = \sigma_{rr} + \sigma_{\theta\theta} - \nu\sigma_{zz} \tag{3}$$

$$= -E\omega^2\left(\frac{1}{2V_S^2} - \frac{1}{V_P^2}\right)\phi_E(z), \tag{4}$$

where V_P and V_S are the low-frequency (Gassmann-limit) P- and S-wave velocities of the formation (from Equations E6–E8 in Appendix E). This is the mechanism shown in Figure 2b.

2.1.2.2. Fluid Infiltration

Corresponding to the mechanism shown in Figure 2a, at low frequencies viscous forces dominate the pore-fluid flow. Combining Darcy's law and the continuity equation yields the diffusion equation for the pore pressure $p_{\text{por}}(r, \omega)$ in the porous formation (Ionov & Maximov, 1996):

$$-i\omega p_{\text{por}} = a^2\nabla_r^2 p_{\text{por}}, \tag{5}$$

$$a^2 = \frac{\kappa_0 K_f}{\eta\phi}, \tag{6}$$

where ∇_r^2 denotes the radial Laplacian and κ_0, η, and ϕ are the static permeability, dynamic viscosity, and porosity, respectively.

The boundary conditions of Equation 5 are as follows. At the borehole wall, we impose pressure continuity, $p_{\text{por}}(R, \omega) = p$, where R is the borehole radius. At large distances, the pore-pressure gradient vanishes, $\lim_{r\to\infty}\partial p_{\text{por}}/\partial r = 0$, consistent with a plane wave in an infinite medium. This far-field condition implies zero fluid flux at infinity and a locally undrained response in the low-frequency limit, for which we prescribe the Biot–Gassmann relation

$$p_{\text{por}}^{\text{ext}}(z) \equiv \lim_{r\to\infty}p_{\text{por}}(r, \omega) = -\frac{1}{3}B\sigma_{ii}(z) = B k_p^2 K \phi_E(z), \tag{7}$$

where σ_{ii} is the sum of the normal components of the wave-induced (perturbation) stress tensor (its trace), K is the undrained bulk modulus from the Gassmann equation (Equations E5, E6), and B is the Skempton coefficient (Equation E4). The key new element in this study is the explicit Biot–Gassmann–consistent far-field condition
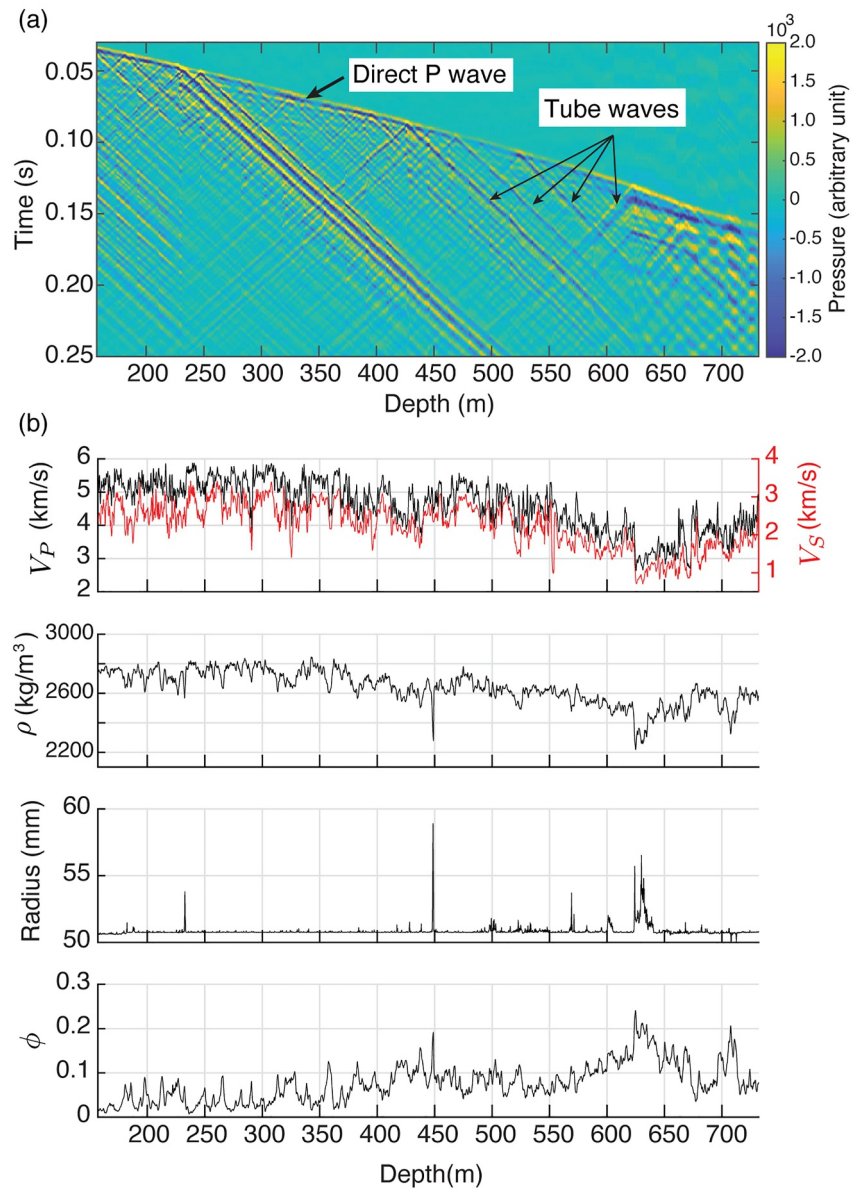
Figure 3. (a) Hydraulic fluid-pressure response at a borehole located within a fault zone, induced by incident P-waves from a pressure source located near the surface. (b) Downhole log data: P-wave velocity (V_P) and S-wave velocity (V_S) from the sonic log, density (ρ) from the density log, borehole radius from the caliper log, and porosity (ϕ) from the neutron log (adopted from Kiguchi et al., 2001).

(Equation 7) written with the Skempton coefficient B. The choice $B = 1$ reduces the condition to the boundary used in Ionov and Maximov (1996).

Solving Equation 5 with the above boundary conditions yields the non-divergent solution

$$p_{\mathrm{por}}(r, \omega) = \left(p - p_{\mathrm{por}}^{\mathrm{ext}}\right) \frac{K_0\left(\sqrt{-i\omega}\, r/a\right)}{K_0\left(\sqrt{-i\omega}\, R/a\right)} + p_{\mathrm{por}}^{\mathrm{ext}}, \qquad (8)$$

where K_0 is the modified Bessel function of the second kind (order zero). From Equation 8,

$$v_{\mathrm{ft}} = -\frac{\kappa_0}{\eta}\frac{\partial p_{\mathrm{por}}}{\partial r}\bigg|_{r=R} \tag{9}$$

$$= -i\omega R\frac{\phi}{K_f}(p - p_{\mathrm{por}}^{\mathrm{ext}})\Phi\left(\sqrt{-i\omega t_f}\right), \tag{10}$$

with $\Phi(w) = w^{-1}K_1(w)/K_0(w)$ and $t_f = R^2\phi\eta/\kappa_0 K_f$.

2.1.3. Governing Equation

Substituting Equations 2, 4, and 10 into Equation 1 gives

$$\frac{\partial}{\partial z}\begin{pmatrix} p \\ v_z \end{pmatrix} = i\omega\begin{pmatrix} 0 & \rho_f \\ K_{\mathrm{eff}}^{-1} & 0 \end{pmatrix}\begin{pmatrix} p \\ v_z \end{pmatrix} + i\omega\begin{pmatrix} 0 \\ \dfrac{2\sigma_{\mathrm{eff}}^{\mathrm{ext}}}{E} - \dfrac{2\phi}{K_f}p_{\mathrm{por}}^{\mathrm{ext}}\Phi\left(\sqrt{-i\omega t_f}\right) \end{pmatrix}, \tag{11}$$

which reduces, if the last source term is neglected, to a one-dimensional fluid system with effective bulk modulus

$$K_{\mathrm{eff}}^{-1} = K_f^{-1} + \mu^{-1} + \frac{2\phi}{K_f}\Phi\left(\sqrt{-i\omega t_f}\right). \tag{12}$$

Here, μ and Φ represent elastic deformation and fluid infiltration. The tube-wave phase velocity is $C_T = \sqrt{K_{\mathrm{eff}}/\rho_f}$ and is generally complex-valued. In the impermeable limit, the last term in Equation 12 vanishes, recovering White's classical result (White, 1983).

2.2. Propagator-Matrix Formulation for the Borehole Response for Multi-Layered Media

2.2.1. Formulation

We recast the governing system (Equation 11) into a propagator-matrix scheme for a stack of N horizontal layers, a standard approach for vertically heterogeneous media (e.g., Aki & Richards, 2002; Gilbert & Backus, 1966). In layer n, the tube-wave potential ϕ_f is given by

$$\phi_{\mathrm{f}}^{(n)}(z) = D_{\mathrm{f}}^{(n)}e^{ik_nz} + U_{\mathrm{f}}^{(n)}e^{-ik_nz}, \tag{13}$$

with tube-wave wavenumber $k_n = \omega/C_T^{(n)}$ and borehole radius r_n (Figure 4). In a source-free interval,

$$p = \rho_f\omega^2\phi_{\mathrm{f}}, \qquad v_z = -i\omega\frac{\partial\phi_{\mathrm{f}}}{\partial z}. \tag{14}$$

The P-wave potential ϕ_E is computed independently (Appendix A) and used as known input.

At the interface $z = z_n$ between layers n and $n + 1$, the interface (continuity) conditions are:

$$p^{(n)} + \Delta p^{(n)} = p^{(n+1)}, \tag{15}$$

$$\pi r_n^2\left\{v_z^{(n)} + \Delta v_z^{(n)}\right\} = \pi r_{n+1}^2 v_z^{(n+1)}. \tag{16}$$

Here $p^{(n)}$ and $v_z^{(n)}$ denote the fields in the absence of sources within layer n, and the discontinuities $\left(\Delta p^{(n)}, \Delta v_z^{(n)}\right)$ collect contributions from the three mechanisms in Figure 2 (derived below).

Using Equations 13 and 14, the interface conditions (Equations 15 and 16) become

$$\mathbf{u}_n = \mathbf{M}_n(z_n)\mathbf{u}_{n+1} + \mathbf{S}_n(z_n), \tag{17}$$
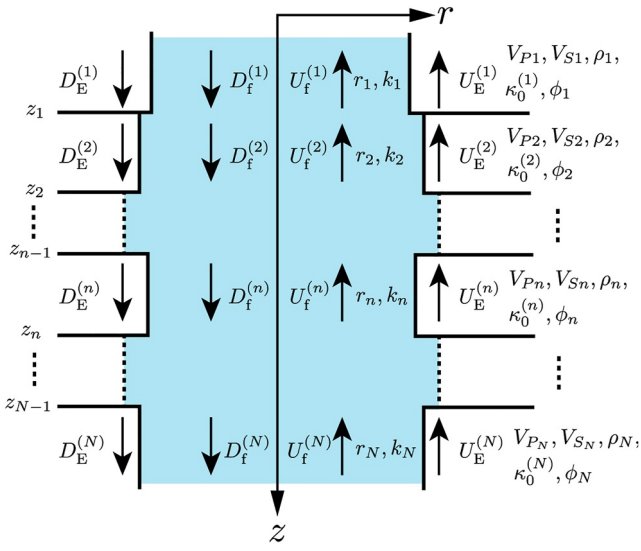
Figure 4. An irregular borehole in a multi-layered poroelastic subsurface. The N-layers are described by their respective parameters and the borehole radius. The upgoing and downgoing potential amplitudes at each layer are indicated as $U_{\mathrm{f}}^{(i)}$ and $D_{\mathrm{f}}^{(i)}$ for the tube wave, and $U_{\mathrm{E}}^{(i)}$ and $D_{\mathrm{E}}^{(i)}$ for the elastic wave.

$$\mathbf{u}_n = \left(U_{\mathrm{f}}^{(n)}, D_{\mathrm{f}}^{(n)}\right)^{\mathrm{T}} \tag{18}$$

with

$$\mathbf{M}_n(z) = \frac{1}{2 r_n^2 k_n} \begin{pmatrix} a_1 e^{i(k_n - k_{n+1})z} & a_2 e^{i(k_n + k_{n+1})z} \\ a_2 e^{-i(k_n + k_{n+1})z} & a_1 e^{-i(k_n - k_{n+1})z} \end{pmatrix}, \tag{19}$$

$$a_1 = r_n^2 k_n + r_{n+1}^2 k_{n+1}, \tag{20}$$

$$a_2 = r_n^2 k_n - r_{n+1}^2 k_{n+1}. \tag{21}$$

and the source vector

$$\mathbf{S}_n(z) = \frac{1}{2\rho_f \omega^2 k_n} \begin{pmatrix} \left\{\Delta v_z^{(n)} \rho_f \omega - k_n \Delta p^{(n)}\right\} e^{ik_n z} \\ -\left\{\Delta v_z^{(n)} \rho_f \omega + k_n \Delta p^{(n)}\right\} e^{-ik_n z} \end{pmatrix}. \tag{22}$$

Successive application of Equation 17 gives

$$\mathbf{u}_1 = \mathbf{M}_T \mathbf{u}_N + \mathbf{S}_T, \tag{23}$$

$$\mathbf{M}_T = \prod_{i=1}^{N-1} \mathbf{M}_i(z_i) \tag{24}$$

with the total source accumulation

$$\mathbf{S}_T = \sum_{j=2}^{N-1} \prod_{i=2}^{j} \mathbf{M}_{i-1}(z_{i-1}) \mathbf{S}_j + \mathbf{S}_1. \tag{25}$$

Case $N = 2$ (single interface): Equations 24 and 25 hold, but the product/sum collapses because there are no interior layers. Furthermore, the depth-accumulated Δ-terms are evaluated with the interface itself as the reference depth (Appendix C; see also Section 3.2).

Radiation conditions and solution: We assume a single downgoing plane P-wave incident from $z = -\infty$ (top) and a semi-infinite half-space below with no external incidence from below. At $z = z_1$ and $z = z_{N-1}$, the boundary vectors equal the homogeneous incident field (evaluated at the boundary) plus outward-only scattered components (Appendix C). These two linear boundary equations, combined with Equation 23, yield a 2×2 system for two unknown boundary amplitudes (conveniently $U_{\mathrm{f}}^{(1)}$ and $D_{\mathrm{f}}^{(N)}$). The amplitudes in any interior layer then follow from Equation 17.

Finally, including the discontinuities, the borehole response in layer n is

$$p(z) = \rho_f \omega^2 \left(D_{\mathrm{f}}^{(n)} e^{ik_n z} + U_{\mathrm{f}}^{(n)} e^{-ik_n z}\right) + \Delta p^{(n)}(z_{n-1}, z), \tag{26}$$

$$v_z(z) = k_n \omega \left(D_{\mathrm{f}}^{(n)} e^{ik_n z} - U_{\mathrm{f}}^{(n)} e^{-ik_n z}\right) + \Delta v_z^{(n)}(z_{n-1}, z), \tag{27}$$

for $z_{n-1} \leq z \leq z_n$, and $2 \leq n \leq N - 1$.

2.2.2. The Discontinuities and Source Terms

2.2.2.1. Calculation of Discontinuities

We can rewrite Equation 11 as

$$\frac{d\mathbf{f}(z)}{dz} = \mathbf{A}(z)\mathbf{f}(z) + \mathbf{g}(z), \tag{28}$$

$$\mathbf{f} = \begin{pmatrix} p \\ v_z \end{pmatrix}, \tag{29}$$

$$\mathbf{A} = i\omega \begin{pmatrix} 0 & \rho_f \\ K_{\text{eff}}^{-1} & 0 \end{pmatrix}, \tag{30}$$

$$\mathbf{g} = i\omega \begin{pmatrix} 0 \\ \dfrac{2\sigma_{\text{eff}}^{\text{ext}}}{E} - \dfrac{2\phi}{K_f} p_{\text{por}}^{\text{ext}} \Phi\left(\sqrt{-i\omega t_f}\right) \end{pmatrix}. \tag{31}$$

The solution can be written as (Aki & Richards, 2002),

$$\mathbf{f}(z) = \mathbf{P}(z, z_0)\,\mathbf{f}(z_0) + \int_{z_0}^{z} \mathbf{P}(z, \zeta)\mathbf{g}(\zeta)d\zeta, \tag{32}$$

where z_0 is a reference depth to calculate the integral and $\mathbf{P}$ is the propagator matrix:

$$\mathbf{P}(z, z_0) = \frac{1}{2} \begin{pmatrix} e^{ik(z-z_0)} + e^{-ik(z-z_0)} & \rho_f C_T\left(e^{ik(z-z_0)} - e^{-ik(z-z_0)}\right) \\ \dfrac{1}{\rho_f C_T}\left(e^{ik(z-z_0)} - e^{-ik(z-z_0)}\right) & e^{ik(z-z_0)} + e^{-ik(z-z_0)} \end{pmatrix}. \tag{33}$$

Comparing Equation 32 with Equations 26 and 27 shows that the integral term yields the discontinuities:

$$\begin{pmatrix} \Delta p(z_0, z) \\ \Delta v_z(z_0, z) \end{pmatrix} = \int_{z_0}^{z} \mathbf{P}(z, \zeta)\mathbf{g}(\zeta)d\zeta. \tag{34}$$

Evaluating Equation 34 gives the explicit relations below.

2.2.2.2. Elastic Deformation

For mechanism shown in Figure 2b, we use

$$\mathbf{g} = \begin{pmatrix} 0 \\ \dfrac{2i\omega\sigma_{\text{eff}}^{\text{ext}}}{E} \end{pmatrix} \tag{35}$$

and with Equations 4 and 34,

$$\Delta p_{\text{E}}^{(n)}(z_{n-1}, z) = -i\omega\rho_f C_T k_p A_P\left\{D_{\text{E}}^{(n)} I_1(z_{n-1}, z) + U_{\text{E}}^{(n)} I_2(z_{n-1}, z)\right\}, \tag{36}$$

$$\Delta v_{\text{E}}^{(n)}(z_{n-1}, z) = -i\omega k_p A_P\left\{D_{\text{E}}^{(n)} I_3(z_{n-1}, z) + U_{\text{E}}^{(n)} I_4(z_{n-1}, z)\right\}, \tag{37}$$

where we define $z_0 = z_{n-1}$ in Equation 34, the subscript "E" on the left-hand sides indicates the contribution due to elastic deformation and all material properties correspond to those at the nth layer. The functions I_1–I_4 characterize the interferences of the waves propagating with P-wave and tube-wave velocities within the layer (Appendix B). The factor A_P in Equations 36 and 37 is the one for the elementary pressure pulse in the borehole (Peng & Toksoz, 1992):

$$A_P = \omega^2 k_p^{-1} \left(\frac{1}{2V_S^2} - \frac{1}{V_P^2} \right).$$

(38)

2.2.2.3. Fluid Infiltration

For mechanism shown in Figure 2a, we retain only the $p_{\text{por}}^{\text{ext}}$ term in Equation 31:

$$\mathbf{g} = \begin{pmatrix} 0 \\ \dfrac{-2i\omega\phi}{K_f} p_{\text{por}}^{\text{ext}} \Phi\left(\sqrt{-i\omega t_f}\right) \end{pmatrix}$$

(39)

which gives with Equations 7 and 34,

$$\Delta p_{\text{ft}}^{(n)}(z_{n-1}, z) = -i\omega \rho_f C_T \frac{\phi \Phi KB}{K_f} k_p^2 \left\{ D_E^{(n)} I_1(z_{n-1}, z) + U_E^{(n)} I_2(z_{n-1}, z) \right\},$$

(40)

$$\Delta v_{\text{ft}}^{(n)}(z_{n-1}, z) = -i\omega \frac{\phi \Phi KB}{K_f} k_p^2 \left\{ D_E^{(n)} I_3(z_{n-1}, z) + U_E^{(n)} I_4(z_{n-1}, z) \right\},$$

(41)

where the subscript "ft" denotes the contribution due to fluid interaction and Φ represents $\Phi\left(\sqrt{-i\omega t_f}\right)$. The dependence on ϕ, Φ, and B highlights sensitivity to porous-formation parameters.

2.2.2.4. Step-Like Change in Borehole Radius

We explicitly include the radius-step mechanism (Figure 2c) as a localized interface source, an effect not treated in Ionov and Maximov (1996). This contribution is absent from the distributed source term $\mathbf{g}$ in Equation 28. The term $\mathbf{g}$ represents depth-distributed forcing via v_r, whereas a radius step is geometric and confined to $z = z_n$. A jump in cross-sectional area creates a local excess/deficit of borehole volume when the wall moves axially with the formation. Kinematically, the ledge moves with axial velocity $v_z^E = -i\omega \, \partial_z \phi_E$ and acts like a short piston face, giving (see hatched area in Figure 2c; Kurkjian et al., 1994)

$$\Delta V = \pi \left(r_{n+1}^2 - r_n^2 \right) v_z^E.$$

(42)

Dividing by the local area yields a cross-section–averaged jump in the borehole-fluid vertical velocity (m/s),

$$\Delta v_q^{(n)} = \frac{\Delta V}{\pi r_n^2} = \frac{r_{n+1}^2 - r_n^2}{r_n^2} k_p \omega \left(D_E^{(n)} e^{ik_p z_n} - U_E^{(n)} e^{-ik_p z_n} \right),$$

(43)

which enters Equation 16 as a velocity discontinuity at $z = z_n$ (while $\Delta p_q^{(n)} = 0$). For a poroelastic contact, the same kinematic form applies with low-frequency elastic moduli (Appendix E); additional vertical flux along the ledge is negligible for realistic radii in our FD tests.

2.2.2.5. Simultaneous Effects

Superposing the three mechanisms,

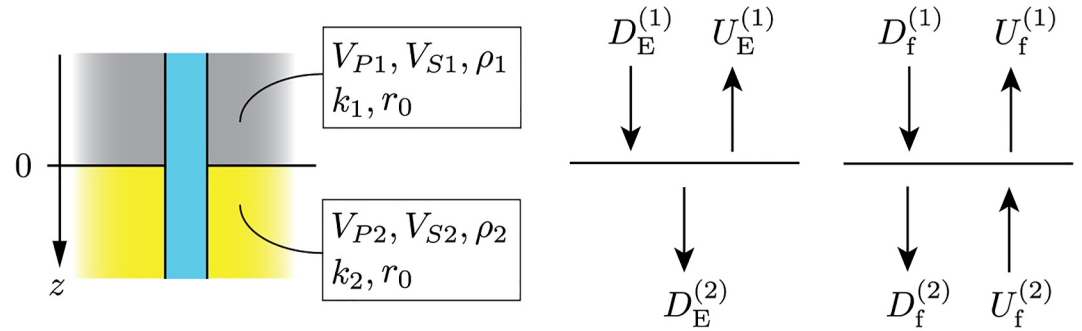$$\Delta p^{(n)}(z_{n-1}, z) = \Delta p_E^{(n)}(z_{n-1}, z) + \Delta p_{\text{ft}}^{(n)}(z_{n-1}, z),$$

(44)

Figure 5. A borehole with a constant radius (r_0) in two elastic half-spaces. The elastic-wave potential amplitudes contain the incident $\left(D_{\mathrm{E}}^{(1)}\right)$, reflected $\left(U_{\mathrm{E}}^{(1)}\right)$, and transmitted $\left(D_{\mathrm{E}}^{(2)}\right)$ waves. The tube-wave potential amplitudes contain the upgoing and the downgoing waves at each layer ($U_{\mathrm{f}}^{(i)}$ and $D_{\mathrm{f}}^{(i)}$).

$$\Delta v_z^{(n)}(z_{n-1}, z) = \Delta v_{\mathrm{E}}^{(n)}(z_{n-1}, z) + \Delta v_{\mathrm{ft}}^{(n)}(z_{n-1}, z) + \Delta v_{\mathrm{q}}^{(n)} \delta(z - z_n). \tag{45}$$

3. Analytical Expression for the Amplitude of the Generated Tube Wave Due To Each Mechanism

Building on the propagator matrix formulation developed in the previous section, we now derive the closed-form expressions for the tube-wave amplitudes generated by each mechanism illustrated in Figure 2. While the propagator matrix scheme computes full waveforms (P and tube waves), isolating tube waves generally requires post-processing. Deriving analytical expressions for key configurations allows us to directly link material properties to the generated tube-wave amplitudes, avoiding full waveform analysis.

3.1. Elastic Layer Boundary

Let us consider a borehole that intersects two elastic half-spaces with the boundary located at $z = 0$ (Figure 5). An incident P wave in the upper half-space $\left(D_{\mathrm{E}}^{(1)}\right)$ produces reflected $\left(U_{\mathrm{E}}^{(1)}\right)$ and transmitted $\left(D_{\mathrm{E}}^{(2)}\right)$ P waves, and their coupling at the boundary generates the tube waves.

For a single interface ($N = 2$) and a constant radius, the source accumulation in Equation 25 vanishes because $z = z_0 = 0$ in Equation 34 (see also Appendix C). The interface relation reduces to

$$\begin{pmatrix} U_{\mathrm{f}}^{(1)} \\ D_{\mathrm{f}}^{(1)} \end{pmatrix} = \mathbf{M}_1(0) \begin{pmatrix} U_{\mathrm{f}}^{(2)} \\ D_{\mathrm{f}}^{(2)} \end{pmatrix}. \tag{46}$$

Radiation conditions are imposed (Appendix C): the boundary vectors equal the homogeneous incident field evaluated at the boundary plus the outward-only scattered components. For the present geometry this yields

$$D_{\mathrm{f}}^{(1)} = \frac{k_{p_1}}{k_1(k_1 - k_{p_1})} A_P^{(1)} D_{\mathrm{E}}^{(1)} + \frac{k_{p_1}}{k_1(k_1 + k_{p_1})} A_P^{(1)} U_{\mathrm{E}}^{(1)}, \tag{47}$$

$$U_{\mathrm{f}}^{(2)} = \frac{k_{p_2}}{k_2(k_2 + k_{p_2})} A_P^{(2)} D_{\mathrm{E}}^{(2)}, \tag{48}$$

where $A_P^{(i)}$ is given by Equation 38 with the properties of half-space i. Note Equation 47 contains an additional term for the upgoing P wave (reflected wave) compared with the homogeneous case (Equation C7). Equations 46–48 determine all four tube-wave amplitudes $U_{\mathrm{f}}^{(1)}, D_{\mathrm{f}}^{(1)}, U_{\mathrm{f}}^{(2)}, D_{\mathrm{f}}^{(2)}$.

As in the homogeneous case (Appendix C), we obtain explicit pressure amplitudes by evaluating Equation 26 at $z = \pm Z$ $(Z > 0)$. In the upper half-space $(z = -Z)$,

$$
\begin{aligned}
p(-Z) = &-\rho_f C_T^{(1)} \omega \frac{2k_1 k_{p_1}}{k_{p_1}^2 - k_1^2} A_P^{(1)} D_{\mathrm{E}}^{(1)} e^{ik_{p_1}(-Z)} \\
&-\rho_f C_T^{(1)} \omega \frac{2k_1 k_{p_1}}{k_{p_1}^2 - k_1^2} A_P^{(1)} R_{\mathrm{E}} D_{\mathrm{E}}^{(1)} e^{-ik_{p_1}(-Z)} \\
&+A_\uparrow e^{-ik_1(-Z)},
\end{aligned} \tag{49}
$$

where the first two terms are, respectively, the downgoing and upgoing P waves, and the last term is the generated upgoing tube wave with amplitude

$$
\begin{aligned}
A_\uparrow = &\rho_f C_T^{(1)} \omega \frac{2k_1 k_{p_1}}{k_{p_1}^2 - k_1^2} A_P^{(1)} \left[\frac{k_2 + k_{p_1}}{k_1 + k_2} R_{\mathrm{E}} + \frac{k_2 - k_{p_1}}{k_1 + k_2} \right] D_{\mathrm{E}}^{(1)} \\
&+\rho_f C_T^{(2)} \omega \frac{2k_2 k_{p_2}}{(k_1 + k_2)(k_2 + k_{p_2})} A_P^{(2)} T_{\mathrm{E}} D_{\mathrm{E}}^{(1)}.
\end{aligned} \tag{50}
$$

In the lower half-space $(z = +Z)$,

$$
\begin{aligned}
p(+Z) = &-\rho_f C_T^{(2)} \omega \frac{2k_2 k_{p_2}}{k_{p_2}^2 - k_2^2} A_P^{(2)} T_{\mathrm{E}} D_{\mathrm{E}}^{(1)} e^{ik_{p_2} Z} \\
&+A_\downarrow e^{ik_2 Z},
\end{aligned} \tag{51}
$$

where the first term is the transmitted P wave and the second is the generated downgoing tube wave with amplitude

$$
\begin{aligned}
A_\downarrow = &\rho_f C_T^{(2)} \omega \frac{2k_2 k_{p_2}}{k_{p_2}^2 - k_2^2} A_P^{(2)} \frac{k_1 + k_{p_2}}{k_1 + k_2} T_{\mathrm{E}} D_{\mathrm{E}}^{(1)} \\
&+\rho_f C_T^{(1)} \omega \frac{2k_1 k_{p_1}}{k_1 + k_2} A_P^{(1)} \left[\frac{R_{\mathrm{E}}}{k_1 + k_{p_1}} + \frac{1}{k_1 - k_{p_1}} \right] D_{\mathrm{E}}^{(1)}.
\end{aligned} \tag{52}
$$

Here R_{E} and T_{E} are, respectively, the P-wave reflection and transmission coefficients defined by the potential amplitudes (Appendix A). In the limiting case of homogeneous media (i.e., $C_T^{(1)} = C_T^{(2)}$, $k_1 = k_2$, $k_{p_1} = k_{p_2}$, $A_P^{(1)} = A_P^{(2)}$, $R_{\mathrm{E}} = 0$), the contrast vanishes and the amplitude becomes zero $(A_\uparrow = A_\downarrow = 0)$, confirming that the phenomenon arises solely from material-parameter contrasts.

3.2. Thin Porous Layer

We next consider tube waves generated by a thin poroelastic layer sandwiched between two identical elastic half-spaces (Figure 6). The top $(n = 1)$ and the bottom $(n = 3)$ layers are elastic, and the middle layer $(n = 2)$ is a porous formation of thickness L_0. When L_0 is small compared with the relevant wavelengths, the tube waves generated at the two boundaries interfere and the response can be approximated by a single upgoing/downgoing tube wave radiated by the thin layer (Li et al., 1994).

In this configuration, the infiltration-driven source terms defined by Equations 40 and 41 are nonzero only in the middle layer $(n = 2)$. Radiation conditions are imposed as in Appendix C. With these constraints, the borehole pressure follows from Equation 23 and evaluation of Equation 26.

Thin-layer (first-order) approximation: Expanding the pressure at $z = -Z$ and $z = L_0 + Z$ $(Z > 0)$ in a Taylor series up to first order in L_0, in the upper half-space,
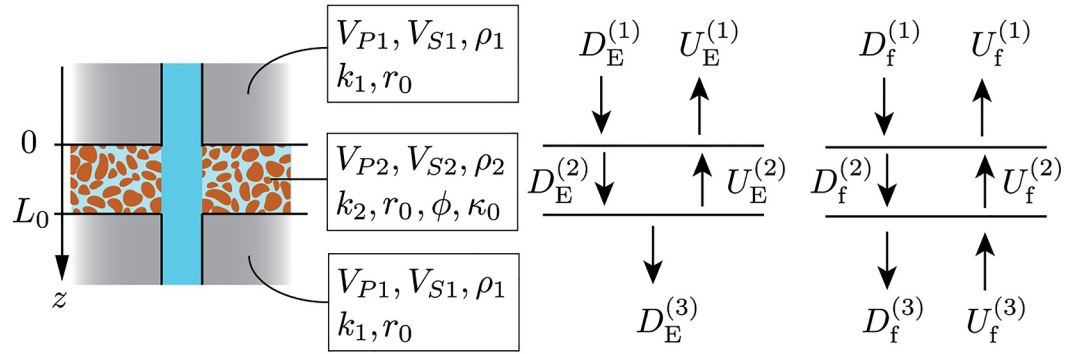
Figure 6. A borehole with a constant radius (r_0) in a porous formation with thickness L_0 sandwiched between two elastic half-spaces with identical properties. $U_E^{(i)}$ and $D_E^{(i)}$ are, respectively, upgoing and downgoing elastic-wave potential amplitudes, and $U_f^{(i)}$ and $D_f^{(i)}$ tube-wave potential amplitudes.

$$
\begin{aligned}
p(-Z) \approx\ & -\rho_f C_T^{(1)} \omega \frac{2 k_1 k_{p_1}}{k_{p_1}^2 - k_1^2} A_P^{(1)} D_E^{(1)} e^{i k_{p_1}(-Z)} \\
& -\rho_f C_T^{(1)} \omega \frac{2 k_1 k_{p_1}}{k_{p_1}^2 - k_1^2} A_P^{(1)} \tilde{R} D_E^{(1)} e^{-i k_{p_1}(-Z)} \\
& + \tilde{A}_\uparrow e^{-i k_1(-Z)},
\end{aligned} \tag{53}
$$

where the three terms are, respectively, the direct P, reflected P, and generated upgoing tube wave. The thin-layer P-wave reflection coefficient is

$$
\tilde{R} = -\frac{i}{2} \frac{k_{p_1}^2 \rho_2^2 - k_{p_2}^2 \rho_1^2}{\rho_1 \rho_2 k_{p_1}} L_0. \tag{54}
$$

The upgoing tube wave amplitude $\tilde{A}_\uparrow$ splits into three terms:

$$
\tilde{A}_\uparrow = \tilde{A}_\uparrow^E + \tilde{A}^{\Delta k} + \tilde{A}^B, \tag{55}
$$

with

$$
\tilde{A}_\uparrow^E = -i\omega \rho_f C_T^{(1)} k_{p_1} \frac{\left(-A_P^{(1)} k_1 \rho_1 \rho_2 + A_P^{(1)} k_1 \rho_2^2 + A_P^{(2)} k_{p_2} \rho_1^2\right) k_{p_1} - A_P^{(1)} k_{p_2}^2 \rho_1^2}{\rho_1 \rho_2 \left(k_{p_1}^2 - k_1^2\right)} D_E^{(1)} L_0, \tag{56}
$$

$$
\tilde{A}^{\Delta k} = -i\omega \rho_f C_T^{(1)} \frac{A_P^{(1)} k_{p_1} \rho_2 k_2^2 - A_P^{(2)} k_{p_2} \rho_1 k_1^2}{\rho_2 \left(k_{p_1}^2 - k_1^2\right)} D_E^{(1)} L_0, \tag{57}
$$

$$
\tilde{A}^B = -i\omega \rho_f C_T^{(1)} \frac{k_{p_2}^2 \rho_1 \phi \Phi K B}{\rho_2 K_f} D_E^{(1)} L_0. \tag{58}
$$

Here $\tilde{A}_\uparrow^E$ is from elastic-contrast terms (A_P, ρ, k_p), $\tilde{A}^{\Delta k}$ arises from the contrast in tube-wave wavenumber (k), and $\tilde{A}^B$ is from the infiltration source term due to the porous layer. Note that k-itself is affected by permeability via Φ and by shear modulus through K_{eff} (Equation 12).
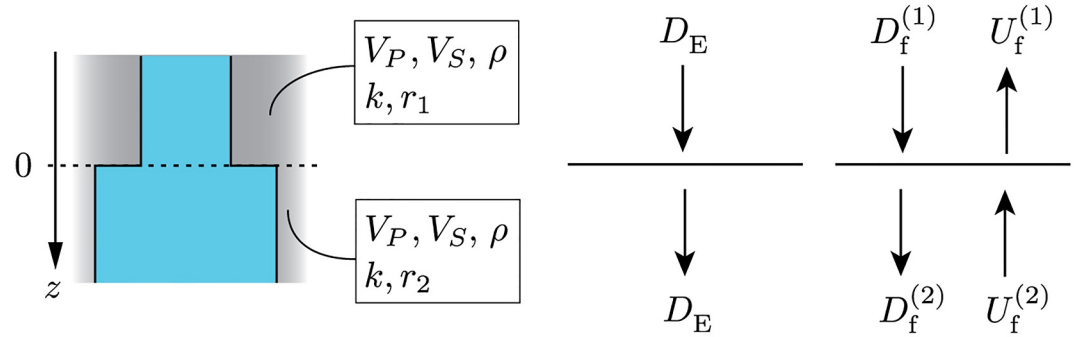
Figure 7. A borehole with an irregular radius located in a homogeneous elastic formation. There is only the incident elastic wave D_E; $U_f^{(i)}$ and $D_f^{(i)}$ are, respectively, upgoing and downgoing tube-wave potential amplitudes.

Similarly, in the lower half-space,

$$
\begin{aligned}
p(L_0 + Z) \approx & -\rho_f C_T^{(1)} \omega \frac{2 k_1 k_{p_1}}{k_{p_1}^2 - k_1^2} A_P^{(1)} \tilde{T} D_E^{(1)} e^{i k_{p_1}(L_0 + Z)} \\
& + \tilde{A}_\downarrow e^{i k_1 (L_0 + Z)},
\end{aligned}
\tag{59}
$$

where each term indicates the transmitted P wave and the generated tube wave. The transmission coefficient $\tilde{T}$ and the downgoing tube wave amplitude $\tilde{A}_\downarrow$ are

$$
\tilde{T} = 1 + \frac{i}{2} \frac{-k_{p_1}^2 \rho_1 \rho_2 + k_{p_1}^2 \rho_2^2 + k_{p_2}^2 \rho_1^2}{\rho_1 \rho_2 k_{p_1}} L_0,
\tag{60}
$$

$$
\tilde{A}_\downarrow = \tilde{A}_\downarrow^E + \tilde{A}^{\Delta k} + \tilde{A}^B,
\tag{61}
$$

where

$$
\tilde{A}_\downarrow^E = -i\omega \rho_f C_T^{(1)} k_{p_1} \frac{\left(A_P^{(1)} k_1 \rho_1 \rho_2 - A_P^{(1)} k_1 \rho_2^2 + A_P^{(2)} k_{p_2} \rho_1^2 \right) k_{p_1} - A_P^{(1)} k_{p_2}^2 \rho_1^2}{\rho_1 \rho_2 \left(k_{p_1}^2 - k_1^2 \right)} D_E^{(1)} L_0.
\tag{62}
$$

The upgoing and downgoing tube-wave amplitudes coincide when $\rho_1 = \rho_2$ (from Equations 56 and 62).

3.3. Step-Like Change in the Borehole Radius

Finally, a single radius step in an otherwise homogeneous elastic formation is considered, corresponding to two layers with a boundary at $z = 0$ (Figure 7). In this case, Equation 23 reduces to

$$
\begin{pmatrix} U_f^{(1)} \\ D_f^{(1)} \end{pmatrix} = \mathbf{M}_1(0) \begin{pmatrix} U_f^{(2)} \\ D_f^{(2)} \end{pmatrix} + \frac{\Delta v_q}{2\omega k} \begin{pmatrix} 1 \\ -1 \end{pmatrix}.
\tag{63}
$$

Evaluating the pressure as in Section 3.1 gives, at $z = \pm Z$ $(Z > 0)$,

$$
\begin{aligned}
p(\pm Z) = & -\rho_f C_T \omega \frac{2 k k_p}{k_p^2 - k^2} A_P D_E e^{i k_p(\pm Z)} \\
& + A_C e^{\pm i k(\pm Z)},
\end{aligned}
\tag{64}
$$

Table 1
Summary of Material Parameters Used in the Semi-Analytical Modeling Approach Developed in This Research and the Finite-Difference (FD) Simulations

Parameter	Semi-analytical approach	FD simulations
Elastic layers	V_P, V_S, ρ	Poroelastic parameters (via parameter-limit approach)[a]
Porous layers[b]	ϕ, κ_0, μ, K_m, K_s, ρ_s	ϕ, κ_0, μ, K_m, K_s, ρ_s
Fluid properties	K_f, ρ_f, ν	K_f, ρ_f, ν
High-frequency tortuosity α_∞ and coefficient n_J[c]	Not used	Required
Skempton coefficient B	Derived from ϕ, K_m, K_s, K_f	Not used explicitly
Borehole irregularities	Specified as 1D variation in borehole radius	Modeled via 2D heterogeneity in poroelastic parameters

[a]To represent acoustic (borehole), elastic, and porous regions consistently, the FD scheme applies the parameter-limit approach of Ou and Wang (2019), treating all media as poroelastic with limiting values derived from the input velocities (V_P, V_S). [b]In the semi-analytical approach, V_P and V_S are calculated from the low-frequency elastic moduli using Gassmann's equation. [c]Parameters α_∞ and n_J are used in the Taylor expansion of the dynamic permeability (Masson et al., 2006); see Appendix D.

that is, the direct P wave plus a symmetric tube-wave term. The generated tube-wave amplitude is

$$A_C = -\rho_f C_T \omega \frac{k_p}{k_p^2 - k^2} \left(\frac{r_1^2 - r_2^2}{r_1^2 + r_2^2} \right) \left(2A_P k_p - k^2 + k_p^2 \right) D_{\text{E}}. \tag{65}$$

This amplitude vanishes when $r_1 = r_2$, showing that the tube wave is generated purely by the area jump at the radius step. Furthermore, its magnitude scales with the relative area contrast $(r_1^2 - r_2^2)/(r_1^2 + r_2^2)$. Equation 65 coincides with the known solution using the quasi-static approximation (Equation 4 in White & Lessenger, 1988).

4. Numerical Modeling Results

4.1. Modeling Framework and Parameter Setup

We validate the semi-analytical approach against finite-difference (FD) solutions of Biot's dynamic poroelastic equations (Appendix D), implemented on a staggered cylindrical grid (e.g., Guan & Hu, 2011; Mittet & Renlie, 1996; Ou & Wang, 2019; Randall, 1991). Following Masson et al. (2006), the formulation captures slow-wave effects through a low-frequency approximation of the dynamic permeability. This regime is valid below the Biot characteristic frequency, where fluid flow is diffusion dominated. It differs from the long-wavelength approximation relative to the borehole radius used in the semi-analytical model: the former concerns frequency-dependent fluid–solid interactions, the latter a geometric scale separation between the wavelength and the borehole diameter. Both conditions are satisfied under typical VSP settings considered here (~200 Hz and borehole radii of a few decimeters), ensuring that the FD solutions provide a reliable benchmark. For completeness, the FD scheme adopts the dynamic permeability model of Johnson et al. (1987), which connects Biot's low- and high-frequency regimes. However, at the frequencies considered in this research, it effectively reduces to the Biot low-frequency limit.

We examine the three configurations illustrated in Figure 2, which represent the primary mechanisms of tube-wave generation considered in this study. For each case, closed-form tube-wave amplitudes were derived in the previous section and are validated against the FD solutions.

Table 1 summarizes the input parameters for the both approaches. The semi-analytical model assumes a 1D depth variation and distinguishes elastic, porous, and fluid-filled borehole domains. Elastic layers are characterized by V_P, V_S, and ρ. Porous layers require frame and grain moduli (K_m, K_s), shear modulus (μ), porosity (ϕ), permeability (κ_0), and grain density (ρ_s), combined with fluid properties (K_f, ν, ρ_f) to compute effective elastic moduli and the Skempton coefficient B via Biot-Gassmann relation (Equations E4, E6, E7, and E8). The FD simulations, in contrast, operate on a 2D cylindrical grid and use the full poroelastic parameter set at each grid point, following Biot's dynamic equations.

4.2. Elastic Layer Boundary

For the two elastic half-spaces shown in Figure 5, we use field-derived material properties from downhole logging data (Figure 3b) near a fault core at approximately 625 m depth (Kiguchi et al., 2001). The upper half-space (representing the hanging wall) has $V_{P1} = 4$ km/s, $V_{S1} = 2$ km/s, $\rho_1 = 2500$ kg/m^3, while the lower half-space (footwall) has $V_{P2} = 3$ km/s, $V_{S2} = 1$ km/s, and $\rho_2 = 2300$ kg/m^3. In this modeling, the borehole radius is set to 0.055 m, and the FD grid spacing is 0.01 m in the radial direction and 0.1 m in the vertical direction. A snapshot of the vertical particle velocity distribution at $t = 0.01$ s is illustrated in Figure 8a, where a unit-amplitude Ricker wavelet of 200 Hz center frequency serves as the vertical stress source representing the incident plane P wave. The initial condition of the FD modeling is set up such that the normal-incident plane P wave starts to propagate downward from 24 m above the elastic impedance boundary (Appendix D). The P wave propagates through the elastic impedance boundary at $z = 0$ m, and consequently, the tube waves are generated, and they propagate 5 m from the boundary (Figure 8a).

A comparison of the borehole fluid pressure from FD modeling with that from the semi-analytical modeling approach developed in this research is presented in Figures 8b and 8c. At ± 10.05 m from the boundary, the two solutions closely match (Figure 8c). We also verify the analytical amplitude derived in Section 3.1. We find that Equations 49–52 accurately reproduce the amplitudes for all observed wave modes (solid black lines in Figure 8c).

A notable characteristic of the results is the opposite polarity between the upgoing and downgoing tube waves generated at the elastic impedance boundary (Figures 8b and 8c). This behavior can be examined more systematically using the new analytical expressions (Equations 49–52), which show how material properties affect the sign of the tube-wave amplitudes. To explore this polarity reversal, we evaluate the amplitude ratio between the incident P wave (the first term in Equation 49) and the generated tube wave (Equations 50 and 52). From Equations 38, 49, 50, 52, and A6, one can see that the amplitude ratio is independent of the frequency. Figure 9 summarizes these amplitude ratios for various impedance contrasts, keeping the upper half-space properties fixed ($V_P = 4$ km/s, $V_p/V_S = 1.7$, $\rho = 2500$ kg/m^3) while varying V_P in the lower half-space from 3 to 5 km/s (with $V_p/V_S = 1.7$ and $\rho = 2500$ kg/m^3). The polarity difference between the upgoing and downgoing tube waves is evident, and the sign of their amplitudes reverses when the lower half-space has a higher seismic velocity than the upper half-space (Figure 9). This phenomenon was initially identified by Peng and Toksoz (1992), who also observed opposite polarities in their approximate solutions. Our developed semi-analytical modeling can accurately capture this polarity reversal.

4.3. Thin Porous Layer

Next, we consider tube waves generated at a thin, poroelastic layer sandwiched between two elastic half-spaces (Figure 6). The poroelastic layer has a thickness of 1 m ($L_0 = 1$ m), permeability of 1 darcy ($\kappa_0 = 9.869 \times 10^{-13}$ m^2), and porosity of 0.3 ($\phi = 0.3$). All material properties are summarized in Table 2. In the FD modeling, we select the grain bulk modulus (K_s), frame bulk modulus (K_m), frame shear modulus (μ), and grain density (ρ_s) for the poroelastic layer such that, in the low-frequency limit (Appendix E), the poroelastic layer has the same effective elastic properties as the surrounding elastic half-spaces. This ensures that tube waves are generated only due to fluid infiltration from the poroelastic layer.

A snapshot of the FD results is shown in Figure 10a, where the poroelastic layer is located between $z = \pm 0.5$m. The incident P wave propagates through this layer, generating tube waves that are visible at $z = \pm 7.5$ m in the borehole. A comparison of the borehole pressures between the FD simulations and the semi-analytical approach (Figures 10b and 10c) indicates excellent agreement. Note that the tube waves generated by fluid infiltration from the porous layer are clearly visible (Figures 10b and 10c). Because there is negligible elastic impedance contrast at the layer boundaries, no reflected P wave is observed. Contrary to the case of an elastic impedance boundary (Section 4.2), the upgoing and downgoing tube waves display the same polarity.

To further quantify these results, we calculate the ratio of tube-wave amplitude to the incident P-wave amplitude (Figure 11). The amplitude ratio from the semi-analytical approach (solid lines) is obtained by isolating the terms associated with the generated tube waves in the algebraic expressions of Equation 26 at $z = -Z$ and $z = L + Z$, following the same procedure as in Section 3.1. For the FD results (open squares), the incident P wave and the
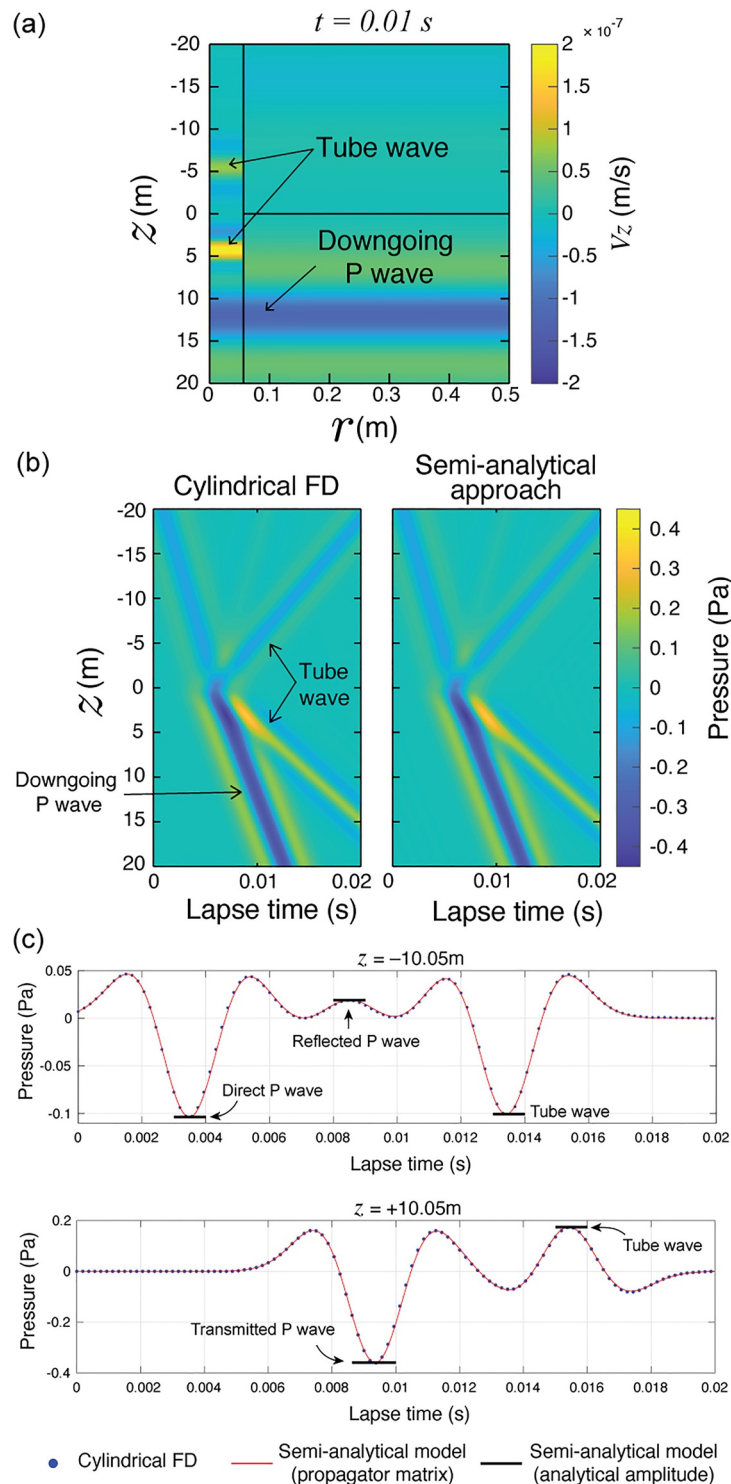
Figure 8. Verification of the semi-analytical modeling approach developed in this study using finite-difference (FD) modeling for a borehole located in two elastic half-spaces (Figure 5). (a) The snapshot of the wavefield (vertical particle velocity) calculated by cylindrical FD method at $t = 0.01$ s, when the downgoing P wave has propagated approximately 10 m below the elastic-layer boundary. The borehole wall is located at $r = 0.055$ m (shown as the black vertical line), and the elastic-layer boundary is indicated by the black horizontal line. (b) Comparison of the pressure waveforms in the borehole calculated by FD and the modeling approach developed in this study. (c) Same as (b) but for a receiver located at ± 10.05 m from the elastic impedance boundary. The red lines are calculated waveforms using the new approach and the propagator matrix method (Equations 23 and 26); the solid black lines denote the analytical amplitudes derived from this approach (Equations 49–52).
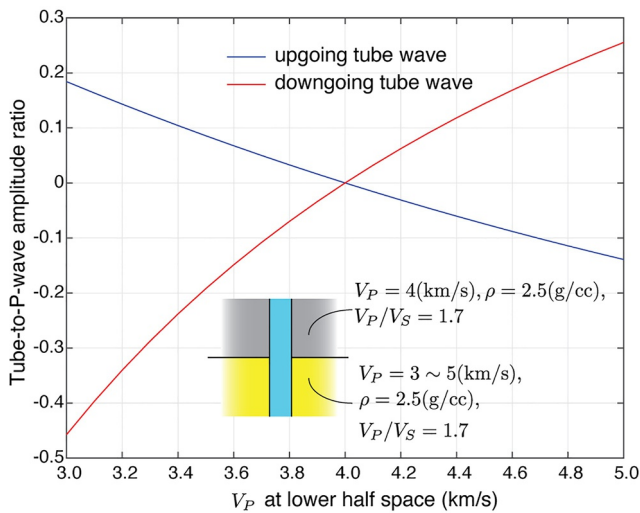
Figure 9. Pressure amplitude of the generated tube wave (Equations 50 and 52) normalized by the pressure amplitude of the incident P wave (the first term in Equation 49), when the borehole is embedded in two elastic half-spaces. A fixed seismic velocity at the upper half-space and varying seismic velocity at the lower space are used.

generated tube wave are separated in the time domain by applying a window, and the tube-wave contribution is isolated by subtracting the waveform obtained without the poroelastic layer from the total response. The tube-to-P-wave amplitude ratio from the FD and the new semi-analytical modeling approach show good agreement, with slight differences likely arising from the numerical dispersion in the FD modeling and/or the quasi-static approximation in the semi-analytical approach.

Notably, this amplitude ratio exhibits a clear frequency dependence and differs between the upgoing and the downgoing tube waves (Figure 11), implying that their time-domain waveforms are not identical. Although earlier studies (e.g., Li et al., 1994) did not address this phenomenon, our results reveal that the amplitude difference between upgoing and downgoing tube waves becomes increasingly pronounced at higher frequencies (above 100 Hz; Figure 11). These observations suggest that, for a porous layer, the effect of asymmetric phase interferences due to the distributed sources (Equations 40 and 41) grows stronger as the layer thickness becomes a larger fraction of the seismic wavelength.

Finally, we demonstrate the importance of incorporating the Skempton coefficient in the boundary condition for the pore pressure (Equation 7) to ensure consistency with the Biot's dynamic poroelastic theory. Figure 12a shows the radial distribution of pore pressure at the center of the poroelastic layer ($z = 0$) at time $t = 0.005$ s, obtained from the FD simulations. This result is compared with the expression $-1/3 \times B\tau_{ii}$, where τ_{ii} is the trace of the total stress tensor calculated from the same FD simulation (see Appendix D). The close agreement confirms that the pore pressure far from the borehole is well approximated by Equation 7. If, instead, one ignores the Skempton coefficient by setting $B = 1$, the resulting pressure is systematically overestimated (Figure 12b). As anticipated in Section 2.1, this validation highlights that including the Skempton coefficient is essential in the semi-analytical modeling to reproduce the behavior predicted by the full Biot simulations.

4.4. Step-Like Change in the Borehole Radius

As a last example, we consider borehole irregularities modeled by an abrupt change in borehole radius (Figure 7). The surrounding medium is homogeneous, with $V_P = 4$ km/s, $V_S = 2$ km/s, and $\rho_1 = 2500$ kg/m^3. In Figure 13, results from the new semi-analytical modeling are compared with the FD simulations for a borehole radius of $r = 0.055$ m in the upper half-space and $r = 0.065$ m in the lower half-space. The two approaches exhibit excellent agreement with each other, and the analytical amplitudes derived from the semi-analytical model accurately match with the FD results.

5. Discussion

5.1. Accuracy of the Developed Model and Comparison With the Previous Approaches

Because tube waves generated due to the interaction of an incident P wave with the porous layers are highly relevant to estimating the fluid-flow properties, they have long been the focus of numerous studies (e.g., Bakku

Table 2
Material Properties Used in Calculating the Fluid-Pressure Response in the Borehole at a Three-Layer Model Including a Thin Porous Layer (Figure 6)

	FD	Semi-analytical modeling (this study)
Porous layer (middle)	$\kappa_0 = 1$ darcy, $\phi = 0.3$, $K_s = 100$ GPa, $K_m = 28.8$ GPa, $\mu = 22.5$ GPa, $\rho_s = 3{,}140$ kg/m^3, $\alpha_\infty = 3$	$\kappa_0 = 1$ darcy, $\phi = 0.3$, $V_P = 5$ km/s, $V_S = 3$ km/s, $\rho = 2{,}500$ kg/m^3, $B = 0.1594$
Elastic layers (top and bottom)	$V_P = 5$ km/s, $V_S = 3$ km/s, $\rho = 2{,}500$ kg/m^3	
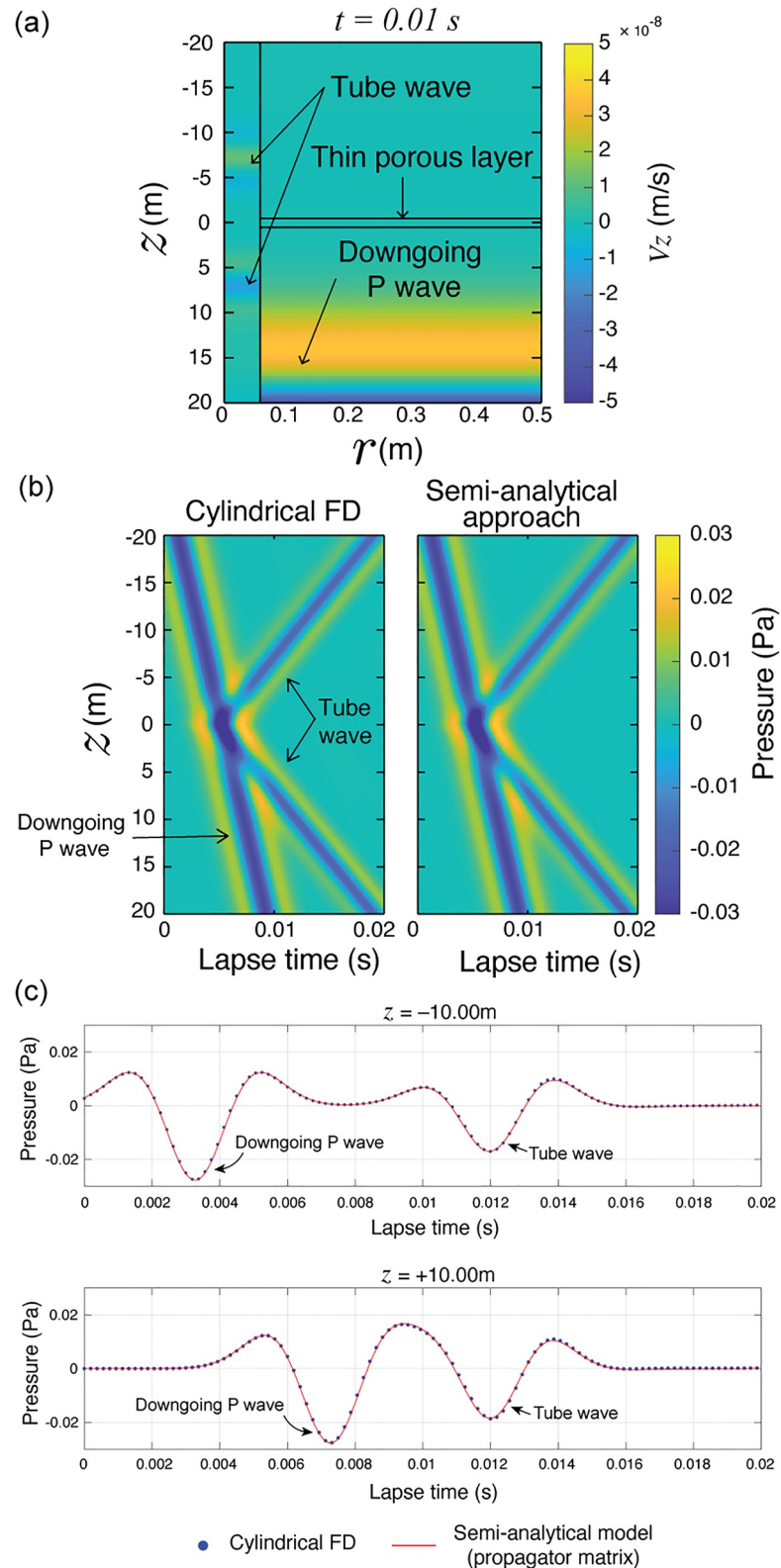
Figure 10. Verification using FD modeling for a borehole through a thin porous formation (Figure 6 and Table 2) with thickness $L_0 = 1$ m. (a) A snapshot of the wavefield calculated by cylindrical (poroelastic) FD. (b) Comparison of the pressure waveforms in the borehole calculated by FD and the semi-analytical approach developed in this study. (c) Same as (b) but for a receiver located at ± 10.00 m distance from the center of the poroelastic layer.
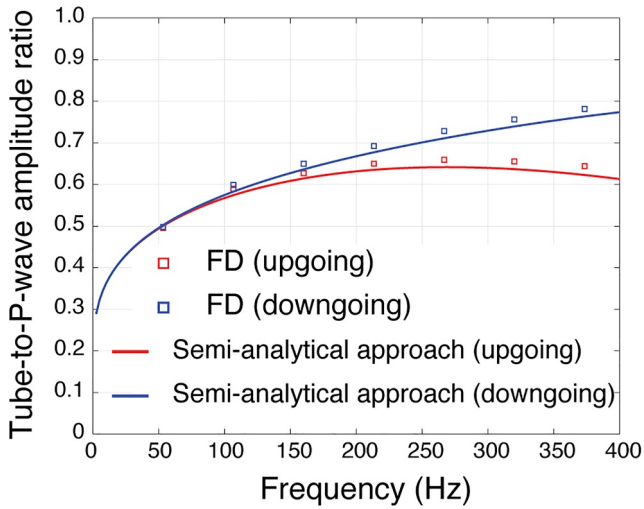
Figure 11. Frequency-dependent tube-to-P-wave amplitude ratio, computed from the borehole pressure response in a model with a porous layer sandwiched between two elastic layers.

et al., 2013; Beydoun et al., 1985; Hardin et al., 1987; Ionov, 2007; Li et al., 1994; Minato, Ghose, Kiguchi, & Tsuji, 2017; Minato, Ghose, Tsuji, et al., 2017). Our model, which simulates a thin porous layer and satisfies the Biot poroelasticity (Section 4.3), proves valuable for analyzing these tube waves. We have additionally derived an analytical solution for the special case of a porous layer, whose thickness is small compared to the seismic wavelength, sandwiched between two elastic layers of identical material properties (Section 3.2). Earlier works also proposed analytical formulas for this scenario; we compare our new expressions with the earlier models.

Using modeling results obtained for the porous layer (Section 4.3), we compare in Figure 14 the analytical amplitudes obtained from different formulations. Previous approaches used the effective-source formulation for the both porous layers (Li et al., 1994; Minato, Ghose, Kiguchi, & Tsuji, 2017) and open fractures (Bakku et al., 2013; Ionov, 2007; Minato, Ghose, Tsuji, et al., 2017). The effective-source model relates the fluid volume at a permeable structure to the tube-wave amplitudes using fluid-continuity equations (Appendix F). Figure 14 shows the ratio of the tube-wave amplitude to the incident P-wave amplitude for a three-layer model (properties presented in Table 2) containing also a thin porous layer of thickness $L_0 = 0.1$ m. Also shown is the amplitude ratio using the earlier model of Li et al. (1994), adapted through the effective-source formulation (Appendix F). For completeness, we also derive the effective-source model based on the pore-pressure diffusion equation incorporated in our semi-analytical modeling (see Appendix F).

The "total" solution (solid red and dashed red lines in Figure 14) directly results from our semi-analytical formulation considering the full boundary condition, including the Skempton coefficient, and validated against the Biot poroelastic simulations. As such, it represents the most complete and accurate description of the tube-wave generation available among all the models considered. The effective-source models (solid black and dashed black lines in Figure 14) deviate substantially from this total solution, even at low frequencies. In contrast, the first-order approximation (blue line; Equation 55 and Equation 61) closely matches the total solution.
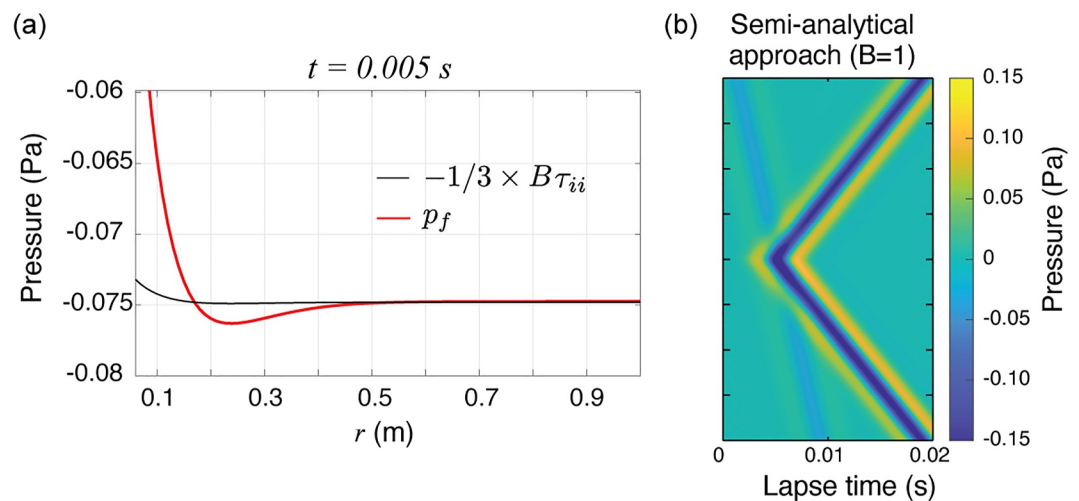
Figure 12. Validation of the far-field pore-pressure boundary condition including Skempton coefficient (B). (a) Distribution of pore pressure p_f (red line) at the center of the poroelastic layer calculated by FD at the lapse time where the P wave propagates through the layer. The black line shows pore-pressure assuming an undrained condition (Equation E3), calculated using the total stress from the FD modeling result and the Skempton coefficient. (b) Borehole-pressure waveforms computed with $B = 1$ (i.e., neglecting the Skempton coefficient); compare with Figure 10b.
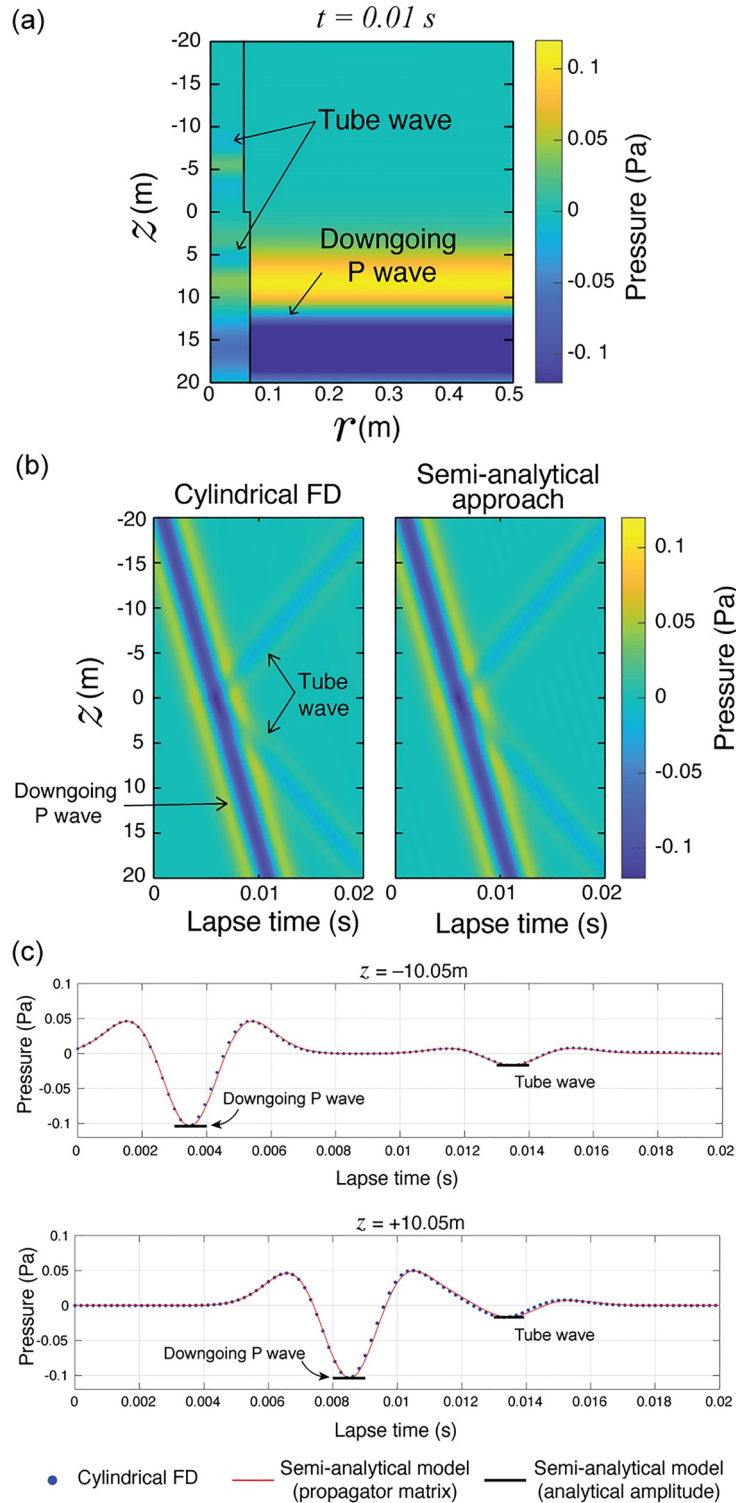
Figure 13. Verification using finite-difference (FD) modeling for an irregular borehole embedded in a homogeneous elastic medium (Figure 7). (a) A snapshot of wavefield calculated by cylindrical FD. (b) Comparison of pressure waveforms at the borehole calculated by FD and those calculated by the semi-analytical approach developed in this study. (c) Same as (b) but for a receiver located at ±10.05 m from the boundary where the radius changes. The red lines are calculated waveforms using our new modeling approach and the propagator matrix method (Equations 23 and 26). The solid black lines are the analytical amplitudes derived from the same approach (Equations 64 and 65).

Figure 14. Comparison of tube-to-P-wave amplitude ratio calculated using various tube-wave generation models for a thin porous layer sandwiched between two elastic layers (Figure 6) where the porous layer thickness $L_0 = 0.1$ m. Note that in first-order approximation, the term associated with the used elastic impedance contrast is zero (i.e., $\tilde{A}_\uparrow^E = \tilde{A}_\do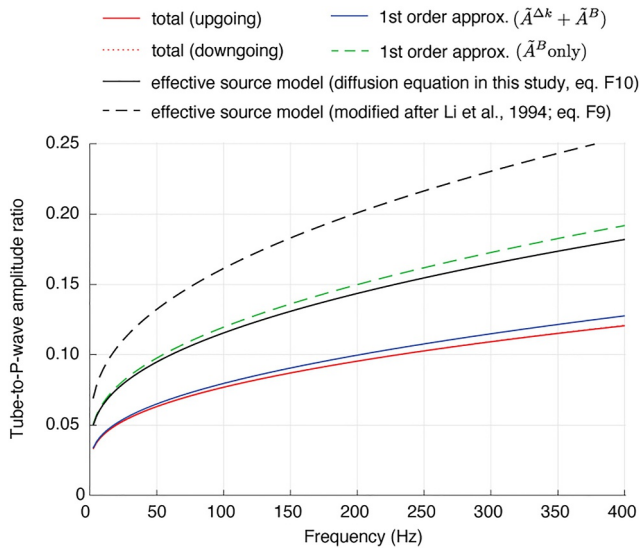wnarrow^E = 0$ in Equations 55 and 61) because of the material properties considered (Table 2). Total: using the theory developed in this study and solved by the propagator matrix method (Equations 23 and 26). Solid red (upgoing) and dashed red (downgoing) lines are on top of each other. 1st order approx: the first-order approximation of the total response in terms of L_0 (Equations 53–62). Effective source model: the amplitude based on the flow volume and the diffusion equation (Appendix F).

The green dashed line in Figure 14, which isolates the contribution from fluid infiltration $\left(\tilde{A}^B\right)$ and omits the change in tube-wave wavenumber $\left(\tilde{A}^{\Delta k}\right)$, converges to the effective-source solution (solid black line) at low frequencies. This highlights a key limitation of the effective-source approach: it neglects the local change in tube-wave velocity (C_T) at the porous layer and the surrounding elastic layers (see Equation 12). It is well known that tube waves can undergo significant reflection and transmission where C_T abruptly changes (e.g., Tezuka et al., 1997). Therefore, if one adopts an effective-source model to compute tube-wave amplitudes, it is important to consider whether the newly generated tube waves experience immediate scattering due to the velocity contrasts. A similar conclusion, but in the context of open fractures, was drawn by Minato and Ghose (2017).

Comparing the two effective-source models, the one adapted from Li et al. (1994) yields a larger amplitude ratio than the diffusion-equation-based model developed here (see solid black and dashed black lines in Figure 14). This difference stems from the specific diffusion equation (Equations F1 and F2) and from the drained bulk modulus approximated by the Reuss average (see Appendix F).

5.2. Elastic Versus Porous Thin Layer

Section 4.3 demonstrates that tube waves generated by fluid filtration across a thin porous layer exhibit a frequency-dependent amplitude without polarity reversal between the downgoing and the upgoing components. To assess whether a purely elastic contrast can produce a similar signature, we repeat the three-layer experiment of Section 4.3, keeping the outer elastic media identical. The middle layer with the same thickness ($L_0 = 1$ m) is replaced with a purely elastic layer (no fluid exchange with the borehole) having reduced seismic velocities ($V_P = 3,500$ m/ s, $V_S = 2100$ m/s). All other parameters (borehole/fluid properties, source–receiver geometry, and processing) are unchanged.

The elastic-layer case shows no polarity reversal between the downgoing and the upgoing tube waves (Figure 15a), consistent with the porous-layer case (Figure 10). The tube-to-P amplitude ratio is frequency dependent in both cases. However, the spectral shapes differ (Figure 15b). For the elastic layer, the ratio increases with frequency almost monotonically over the analyzed frequency range. In contrast, the porous layer exhibits a nonlinear frequency response. In this model, the porous case shows smaller variation of the amplitude ratio across the frequency band. Accordingly, its tube-wave waveform closely follows the incident P-wave in the time domain, whereas in the elastic case the waveform resembles the time derivative. This behavior is consistent with $\tilde{A}^B = 0$ and $-i\omega$ factors in $\tilde{A}_\uparrow^E + \tilde{A}^{\Delta k}$ in the approximate solutions (Equations 53–58) with real-valued C_T.

These results suggest that the polarity alone does not discriminate porous thin layers from elastic thin layers of the same thickness. Spectral analysis is, therefore, useful to investigate the underlying tube-wave generation mechanisms.

5.3. Applicability to Fractured Media

In this study, we exclude tube-wave generation due to open fractures. Such fractures have been modeled as a thin layer of viscous fluid sandwiched between two elastic layers (Bakku et al., 2013; Ionov, 2007; Minato, Ghose, Tsuji, et al., 2017). Open fractures exist throughout the survey depth in the field example shown in Introduction (Figure 3). The model developed in this study can calculate the pressure response of fractured media, provided such fractured media can be approximated by porous layers having appropriate porosity and permeability. In this regard, Minato, Ghose, Kiguchi, and Tsuji (2017) attempted to relate the parameters of a thin porous layer model with those of the open fracture model, assuming the presence of multiple fractures. However, the models
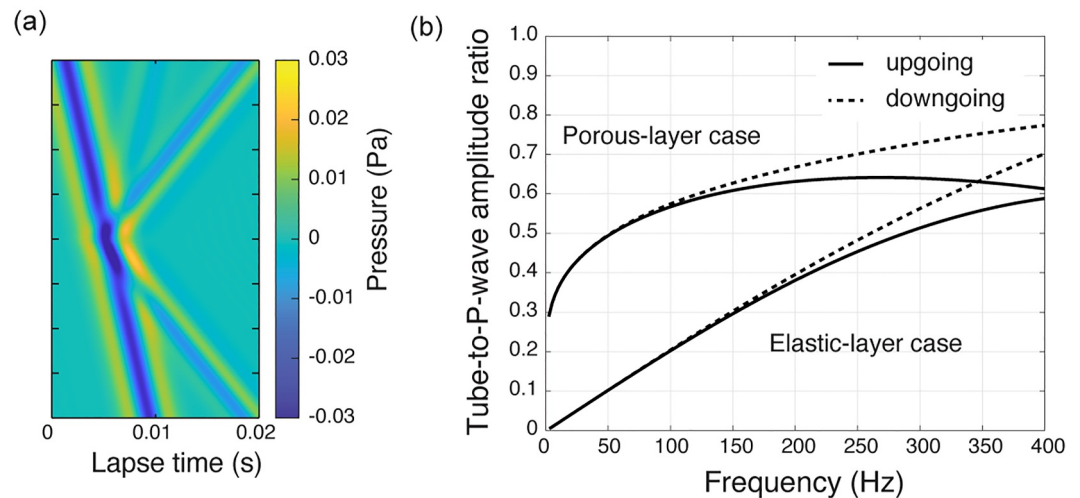
Figure 15. (a) Borehole pressure waveforms computed with the semi-analytical method for the model of Figure 10a, with the porous layer replaced by a purely elastic layer of reduced velocities. (b) Tube-to-P amplitude ratio for the elastic case and, for reference, the porous case (same as Figure 11).

discussed are based on the effective-source formulation. We find that the absence of a localized difference in tube-wave velocity in the effective-source model results in a large deviation from the more accurate semi-analytical solution developed in this study, which has been validated against full Biot poroelastic simulations (Figure 14). Therefore, it remains an open question how tube-wave generation at open fractures can be accurately incorporated into the semi-analytical framework, particularly in the presence of elastic heterogeneity and borehole irregularities.

5.4. Computational Efficiency and Future Inversion Applications

The numerical modeling framework developed in this study also offers promising opportunities for future applications. For example, the simulation involving a poroelastic layer between elastic layers (Figure 10b) completes in roughly one second using the new semi-analytical modeling approach, which is implemented in MATLAB with propagator matrix method. In contrast, the corresponding FD simulation, implemented in Julia, takes about 300 s. Both simulations were run on the same computer, a MacBook Pro with an M1 Max processor and 64 GB of RAM. This significant gain in computational efficiency, in addition to accuracy, highlights the potential of the semi-analytical approach for applications that require repeated forward modeling. In particular, it may enable methods such as full-waveform inversion (FWI) including Bayesian formulations that aim to quantify uncertainty through model-space sampling (e.g., Hunziker et al., 2020; Gebraad et al., 2020, and references therein). Although such inversion strategies remain computationally demanding, the speed of the present method provides a practical foundation for exploring them in future work.

6. Conclusion

Hydrophone VSP can monitor efficiently the hydraulic permeability of an underground porous layer using tube waves. To elucidate the dynamic interactions between borehole fluid and porous formations, we have developed a theoretical framework for computing the pressure response in an irregular-radius borehole embedded in layered poroelastic media and subjected to a normally incident plane P wave. Using a propagator-matrix formulation, we derive closed-form expressions for the amplitudes of tube waves generated by three primary mechanisms: (a) an elastic impedance contrast at layer boundaries, (b) infiltration at a thin poroelastic layer, and (c) a step-like change in the borehole radius. Our semi-analytical modeling approach exhibits excellent agreement with the fully coupled Biot poroelastic simulations. Notably, we demonstrate that the upgoing and the downgoing tube waves at an elastic boundary have opposite polarities, whereas tube waves generated by a thin porous layer show marked frequency dependence and different upgoing/downgoing waveforms. Further comparison with earlier effective-source models reveals that the past approaches

neglect local changes in the tube-wave velocity at the porous layer, causing inconsistencies with the Biot solutions.

By incorporating all three mechanisms into a unified framework, the analytical solutions and modeling approach introduced in this study enable fast and accurate computation of the borehole pressure responses. This capability bridges a critical gap between the current practice of qualitatively interpreting the tube-wave generation—often based on visual correlations with the geological features—and the more rigorous, quantitative assessments achievable through full-scale poroelastic simulations. We are currently processing field VSP data from a fault zone; those results will help assess how effectively hydrophone VSP can capture and monitor the hydraulic properties in faulted environments.

Appendix A: Potential Amplitudes of a Normally Incident Plane P Wave at a Stack of Layers

In this study, we consider the displacement potential of the external elastic waves in the form of $\phi_E(z) = D_E \exp(ik_p z) + U_E \exp(-ik_p z)$. Calculating the potential amplitudes in a stack of elastic layers due to a normally incident plane P wave is trivial, and one can find the solution elsewhere. In order to replicate the analytical tube-wave amplitude derived in this study (Section 4), we briefly summarize the solution in this appendix, using the same notation as in the main text.

First, the vertical velocity and the normal stress are derived from the potential as, $v_z^E = -i\omega \partial \phi_E / \partial z$ and $\sigma_{zz} = -\rho \omega^2 \phi_E$, respectively. Considering the continuity of v_z^E and σ_{zz} at the n-th boundary, the potential-amplitude vector of the plane P wave, $\mathbf{u}_n^E = \left(U_E^{(n)}, D_E^{(n)} \right)^T$, obeys the following relation:

$$\mathbf{u}_n^E = \mathbf{M}_n^E(z_n) \mathbf{u}_{n+1}^E, \tag{A1}$$

where the matrix $\mathbf{M}_n^E$ is defined as

$$\mathbf{M}_n^E(z) = \frac{1}{2} \begin{pmatrix} a_1^E e^{i(k_{p_n} - k_{p_{n+1}})z} & a_2^E e^{i(k_{p_n} + k_{p_{n+1}})z} \\ a_2^E e^{-i(k_{p_n} - k_{p_{n+1}})z} & a_1^E e^{-i(k_{p_n} + k_{p_{n+1}})z} \end{pmatrix}, \tag{A2}$$

$$a_1^E = \frac{\rho_{n+1}}{\rho_n} + \frac{k_{p_{n+1}}}{k_{p_n}}, \tag{A3}$$

$$a_2^E = \frac{\rho_{n+1}}{\rho_n} - \frac{k_{p_{n+1}}}{k_{p_n}}. \tag{A4}$$

Successively applying Equation A1, we obtain the following relation:

$$\begin{aligned} \mathbf{u}_1^E &= \prod_{i=1}^{N-1} \mathbf{M}_i^E(z_i) \mathbf{u}_N^E \\ &= \mathbf{M}_T^E \mathbf{u}_N^E. \end{aligned} \tag{A5}$$

We consider a radiation condition for an infinite half-space at the top and at the bottom layers. The condition can be represented as $\mathbf{u}_1^E = \left(U_E^{(1)}, D_E^{(1)} \right)^T$ and $\mathbf{u}_N^E = \left(0, D_E^{(N)} \right)^T$. We solve Equation A5 for $U_E^{(1)}$ and $D_E^{(N)}$ with a known value for $D_E^{(1)}$ (incident wave). The amplitudes for all layers can be obtained from Equation A1.

The reflection and transmission coefficients (R_E, T_E) for a downgoing incident wave are derived considering $N = 2$, $\mathbf{u}_1^E = (R_E, 1)^T$, and $\mathbf{u}_2^E = (0, T_E)^T$:

$$R_{\mathrm{E}} = \frac{\rho_2 k_{p_1} - \rho_1 k_{p_2}}{\rho_1 k_{p_2} + \rho_2 k_{p_1}}$$

$$T_{\mathrm{E}} = \frac{2\rho_1 k_{p_1}}{\rho_1 k_{p_2} + \rho_2 k_{p_1}}. \tag{A6}$$

Appendix B: Functions I_1, I_2, I_3 and I_4

The functions I_1–I_4 in deriving the discontinuities (Sections 2.2.2.2 and 2.2.2.3) are defined as

$$I_1(z_{n-1}, z) = \int_{z_{n-1}}^{z} \left\{ e^{ik_n(z_n - \zeta)} - e^{-ik_n(z_n - \zeta)} \right\} e^{ik_p \zeta} d\zeta, \tag{B1}$$

$$I_2(z_{n-1}, z) = \int_{z_{n-1}}^{z} \left\{ e^{ik_n(z_n - \zeta)} - e^{-ik_n(z_n - \zeta)} \right\} e^{-ik_p \zeta} d\zeta, \tag{B2}$$

$$I_3(z_{n-1}, z) = \int_{z_{n-1}}^{z} \left\{ e^{ik_n(z_n - \zeta)} + e^{-ik_n(z_n - \zeta)} \right\} e^{ik_p \zeta} d\zeta, \tag{B3}$$

$$I_4(z_{n-1}, z) = \int_{z_{n-1}}^{z} \left\{ e^{ik_n(z_n - \zeta)} + e^{-ik_n(z_n - \zeta)} \right\} e^{-ik_p \zeta} d\zeta. \tag{B4}$$

These functions are originated from the integral for the source term along the depth direction (Equation 34) and characterize the interferences of the waves propagating with P-wave and tube-wave velocities. By evaluating the integral, these functions reduce to the following relationships:

$$I_1(z_{n-1}, z) = \frac{e^{ik_n z}}{i(-k_n + k_{p_n})} \left\{ e^{i(-k_n + k_{p_n})z} - e^{i(-k_n + k_{p_n})z_{n-1}} \right\}$$
$$- \frac{e^{-ik_n z}}{i(k_n + k_{p_n})} \left\{ e^{i(k_n + k_{p_n})z} - e^{i(k_n + k_{p_n})z_{n-1}} \right\}, \tag{B5}$$

$$I_2(z_{n-1}, z) = \frac{e^{ik_n z}}{i(-k_n - k_{p_n})} \left\{ e^{i(-k_n - k_{p_n})z} - e^{i(-k_n - k_{p_n})z_{n-1}} \right\}$$
$$- \frac{e^{-ik_n z}}{i(k_n - k_{p_n})} \left\{ e^{i(k_n - k_{p_n})z} - e^{i(k_n - k_{p_n})z_{n-1}} \right\}, \tag{B6}$$

$$I_3(z_{n-1}, z) = \frac{e^{ik_n z}}{i(-k_n + k_{p_n})} \left\{ e^{i(-k_n + k_{p_n})z} - e^{i(-k_n + k_{p_n})z_{n-1}} \right\}$$
$$+ \frac{e^{-ik_n z}}{i(k_n + k_{p_n})} \left\{ e^{i(k_n + k_{p_n})z} - e^{i(k_n + k_{p_n})z_{n-1}} \right\}, \tag{B7}$$

$$I_4(z_{n-1}, z) = \frac{e^{ik_n z}}{i(-k_n - k_{p_n})} \left\{ e^{i(-k_n - k_{p_n})z} - e^{i(-k_n - k_{p_n})z_{n-1}} \right\}$$
$$+ \frac{e^{-ik_n z}}{i(k_n - k_{p_n})} \left\{ e^{i(k_n - k_{p_n})z} - e^{i(k_n - k_{p_n})z_{n-1}} \right\}. \tag{B8}$$

In the special case where we consider the contribution from infinity (i.e., $z_{n-1} = -\infty$), Equations B5–B8 can be written as

$$I_1(-\infty, z) = \frac{2k}{i(k_p^2 - k^2)} e^{ik_p z}, \tag{B9}$$

$$I_2(-\infty, z) = \frac{2k}{i(k_p^2 - k^2)} e^{-ik_p z}, \tag{B10}$$

$$I_3(-\infty, z) = \frac{2k_p}{i(k_p^2 - k^2)} e^{ik_p z}, \tag{B11}$$

$$I_4(-\infty, z) = \frac{-2k_p}{i(k_p^2 - k^2)} e^{-ik_p z}, \tag{B12}$$

where we ignore the terms associated with the infinite delay time (White, 1953).

Appendix C: Radiation Conditions and Tube-Wave Potentials in a Homogeneous Elastic Medium

We derive the tube-wave potential amplitudes $\left(U_{\mathrm{f}}, D_{\mathrm{f}}\right)$ for a downgoing plane P wave in a homogeneous elastic medium and show how these expressions represent the radiation conditions used at the top/bottom half-spaces in the propagator-matrix formulation (Section 2.2).

C1. Tube-Wave Amplitudes for an Infinite Homogeneous Medium

Choose an arbitrary reference depth z_1 and split the medium at $z = z_1$ with amplitude vectors $\mathbf{u}_1 = \left(U_{\mathrm{f}}^{(1)}, D_{\mathrm{f}}^{(1)}\right)^{\mathrm{T}}$ and $\mathbf{u}_2 = \left(U_{\mathrm{f}}^{(2)}, D_{\mathrm{f}}^{(2)}\right)^{\mathrm{T}}$ (Figure C1). From the interface conditions (Equation 17),

$$\mathbf{u}_1 = \mathbf{M}_1(z_1)\, \mathbf{u}_2 + \mathbf{S}_1(z_1).$$

In a homogeneous medium, $\mathbf{M}_1(z_1) = \mathbf{I}$. The source accumulation measured from the reference point vanishes at that point,

$$\mathbf{S}_1(z_1) = \begin{pmatrix} \Delta p(z_1, z_1) \\ \Delta v_z(z_1, z_1) \end{pmatrix} = \int_{z_1}^{z_1} \mathbf{P}(z_1, \zeta)\, \mathbf{g}(\zeta)\, d\zeta = \mathbf{0} \quad \text{(Equation 34)}.$$

Hence, $\mathbf{u}_1 = \mathbf{u}_2$; the tube-wave amplitudes are independent of the choice of z_1.

In an infinite homogeneous medium with a given elastic incidence (e.g., a downgoing plane P wave from $z = -\infty$), the total field corresponds solely to that elastic excitation, with no external tube-wave source. In our formulation, this condition is imposed at z_1 by
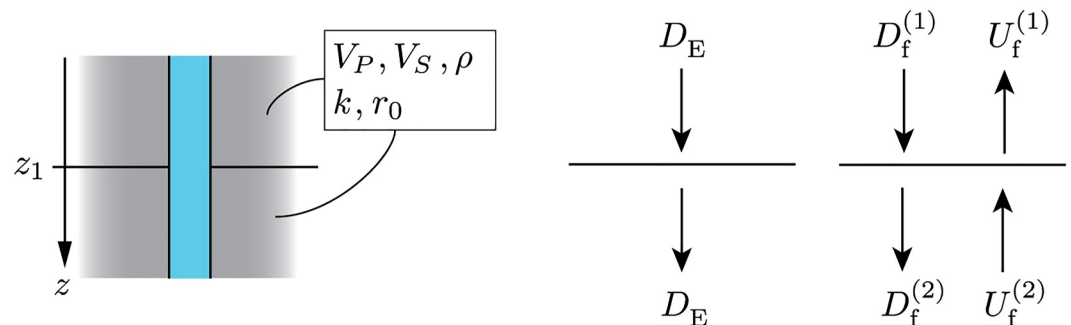

Figure C1. A borehole with a constant radius (r_0) embedded in a homogeneous elastic medium. The elastic-wave potential amplitude contains the downgoing incident wave only (D_{E}). The tube-wave potential amplitudes contain upgoing and downgoing waves at each layer ($U_{\mathrm{f}}^{(i)}$ and $D_{\mathrm{f}}^{(i)}$).

$$\left.\begin{pmatrix} p \\ v_z \end{pmatrix}\right|_{z=z_1} = \begin{pmatrix} \Delta p_E(-\infty, z_1) \\ \Delta v_E(-\infty, z_1) \end{pmatrix}, \tag{C1}$$

where $\Delta p_E, \Delta v_E$ are given by Equations 36 and 37. For a single downgoing incident P wave, we set $U_E = 0$ and retain D_E, then the required integrals $I_{1-4}(-\infty, z_1)$ appear in Equations B9–B12.

In a source-free interval (Equations 26 and 27 without Δ-terms), we get

$$p(z) = \rho_f \omega^2 \left(D_f e^{ikz} + U_f e^{-ikz} \right) \tag{C2}$$

$$v_z(z) = k\omega \left(D_f e^{ikz} - U_f e^{-ikz} \right). \tag{C3}$$

Evaluating Equations C2–C3 at $z = z_1$ and solving for D_f and U_f yields

$$D_f(z_1) = \frac{1}{2} e^{-ikz_1} \left[\frac{p(z_1)}{\rho_f \omega^2} + \frac{v_z(z_1)}{k\omega} \right], \tag{C4}$$

$$U_f(z_1) = \frac{1}{2} e^{+ikz_1} \left[\frac{p(z_1)}{\rho_f \omega^2} - \frac{v_z(z_1)}{k\omega} \right]. \tag{C5}$$

Substituting $p(z_1) = \Delta p_E(-\infty, z_1)$ and $v_z(z_1) = \Delta v_E(-\infty, z_1)$ with $U_E = 0$ yields the explicit expressions

$$U_f^{(H)} = U_f^{(1)} = U_f^{(2)} = \frac{k_p}{k(k + k_p)} A_P \, D_E \, e^{i(k + k_p)z_1}, \tag{C6}$$

$$D_f^{(H)} = D_f^{(1)} = D_f^{(2)} = \frac{k_p}{k(k - k_p)} A_P \, D_E \, e^{-i(k - k_p)z_1}, \tag{C7}$$

where $A_P = \omega^2 k_p^{-1} \left(\frac{1}{2V_S^2} - \frac{1}{V_P^2} \right)$.

C2. Recovery of the Plane-P Pressure by Evaluating at $z_1 \pm Z$

To verify that Equations C6 and C7 represent the downgoing plane-P response, we evaluate the pressure at $z = z_1 \pm Z$ with $Z > 0$. From Equation 26 we obtain, above the reference depth ($z = z_1 - Z$),

$$\begin{aligned} p(z_1 - Z) &= \rho_f \omega^2 \left(D_f^{(H)} e^{ik(z_1 - Z)} + U_f^{(H)} e^{-ik(z_1 - Z)} \right) + \Delta p_E^{(1)}(z_1, z_1 - Z) \\ &= -\rho_f C_T \omega \, \frac{2kk_p}{k_p^2 - k^2} \, A_P \, D_E \, e^{ik_p(z_1 - Z)}, \end{aligned} \tag{C8}$$

and below it ($z = z_1 + Z$),

$$\begin{aligned} p(z_1 + Z) &= \rho_f \omega^2 \left(D_f^{(H)} e^{ik(z_1 + Z)} + U_f^{(H)} e^{-ik(z_1 + Z)} \right) + \Delta p_E^{(2)}(z_1, z_1 + Z) \\ &= -\rho_f C_T \omega \, \frac{2kk_p}{k_p^2 - k^2} \, A_P \, D_E \, e^{ik_p(z_1 + Z)}. \end{aligned} \tag{C9}$$

These expressions show that interference of upgoing/downgoing tube waves together with the depth-distributed source leaves a single downgoing P-wave response. The amplitude matches known results for a plane P wave at low frequency (White, 1983, eq. 5.36); see also (Schoenberg, 1986, eqs. 5 and C-5).

C3. Radiation Conditions for an N-Layer Stack

Let $\mathbf{u}_1 = \left(U_f^{(1)}, D_f^{(1)} \right)^T$ and $\mathbf{u}_N = \left(U_f^{(N)}, D_f^{(N)} \right)^T$ be the tube-wave amplitude vectors at the top (z_1) and bottom (z_{N-1}). Decompose each into an incident (homogeneous) part and a scattered part:

$$\mathbf{u}_1 = \mathbf{u}_1^{\text{inc}} + \mathbf{u}_1^{\text{sc}}, \tag{C10}$$

$$\mathbf{u}_N = \mathbf{u}_N^{\text{inc}} + \mathbf{u}_N^{\text{sc}}. \tag{C11}$$

The incident components are obtained from the homogeneous solutions (Equations C6–C7) evaluated at the actual boundary depths, using the local parameters (at $z = z_1$ and $z = z_{N-1}$):

$$\mathbf{u}_1^{\text{inc}} = \begin{pmatrix} U_f^{(H)}(z_1) \\ D_f^{(H)}(z_1) \end{pmatrix}, \tag{C12}$$

$$\mathbf{u}_N^{\text{inc}} = \begin{pmatrix} U_f^{(H)}(z_{N-1}) \\ D_f^{(H)}(z_{N-1}) \end{pmatrix}. \tag{C13}$$

The scattered components satisfy the radiation conditions, so that only the outward-propagating term is retained at each boundary:

$$\mathbf{u}_1^{\text{sc}} = \begin{pmatrix} U_f^{(1),\text{sc}} \\ 0 \end{pmatrix}, \tag{C14}$$

$$\mathbf{u}_N^{\text{sc}} = \begin{pmatrix} 0 \\ D_f^{(N),\text{sc}} \end{pmatrix}. \tag{C15}$$

Combining the incident and scattered parts gives the total boundary amplitudes:

$$\mathbf{u}_1 = \begin{pmatrix} U_f^{(1)} \\ D_f^{(H)}(z_1) \end{pmatrix}, \tag{C16}$$

$$\mathbf{u}_N = \begin{pmatrix} U_f^{(H)}(z_{N-1}) \\ D_f^{(N)} \end{pmatrix}. \tag{C17}$$

Therefore, the unknowns in this formulation are $U_f^{(1)}$ and $D_f^{(N)}$. Substituting these expressions into the global relation $\mathbf{u}_1 = \mathbf{M}_T \, \mathbf{u}_N + \mathbf{S}_T$ (Equation 23) yields the 2×2 linear system

$$\begin{pmatrix} U_f^{(1)} \\ D_f^{(H)}(z_1) \end{pmatrix} = \mathbf{M}_T \begin{pmatrix} U_f^{(H)}(z_{N-1}) \\ D_f^{(N)} \end{pmatrix} + \mathbf{S}_T. \tag{C18}$$

This system can be solved directly for $U_f^{(1)}$ and $D_f^{(N)}$. The amplitudes in interior layers then follow from Equation 17.

Appendix D: Implementation of Biot's Poroelasticity in a Cylindrical Finite-Difference Scheme

In this research, we validate our semi-analytical modeling approach using numerical solutions to Biot's dynamic poroelastic equations. The simulations are performed in a cylindrical coordinate system using a staggered-grid finite-difference (FD) method. The governing equations are based on the theory of linear poroelasticity originally developed by Biot (1956b); Biot (1956a, 1962).

The stress-strain relation under azimuthal symmetry can be written as (e.g., Ou & Wang, 2019; Sidler et al., 2014):

$$\dot{p_f} = -C\left(\frac{v_r^{(u)}}{r} + \frac{\partial v_r^{(u)}}{\partial r} + \frac{\partial v_z^{(u)}}{\partial z}\right) - M\left(\frac{v_r^{(w)}}{r} + \frac{\partial v_r^{(w)}}{\partial r} + \frac{\partial v_z^{(w)}}{\partial z}\right), \tag{D1}$$

$$\dot{\tau_{rz}} = \mu\left(\frac{\partial v_z^{(u)}}{\partial r} + \frac{\partial v_r^{(u)}}{\partial z}\right), \tag{D2}$$

$$\dot{\tau_{rr}} = (H - 2\mu)\left(\frac{v_r^{(u)}}{r} + \frac{\partial v_z^{(u)}}{\partial z}\right) + H\frac{\partial v_r^{(u)}}{\partial r} + C\left(\frac{v_r^{(w)}}{r} + \frac{\partial v_r^{(w)}}{\partial r} + \frac{\partial v_z^{(w)}}{\partial z}\right), \tag{D3}$$

$$\dot{\tau_{zz}} = (H - 2\mu)\left(\frac{v_r^{(u)}}{r} + \frac{\partial v_r^{(u)}}{\partial r}\right) + H\frac{\partial v_z^{(u)}}{\partial z} + C\left(\frac{v_r^{(w)}}{r} + \frac{\partial v_r^{(w)}}{\partial r} + \frac{\partial v_z^{(w)}}{\partial z}\right), \tag{D4}$$

$$\dot{\tau_{\theta\theta}} = (H - 2\mu)\left(\frac{\partial v_z^{(u)}}{\partial z} + \frac{\partial v_r^{(u)}}{\partial r}\right) + H\frac{v_r^{(u)}}{r} + C\left(\frac{v_r^{(w)}}{r} + \frac{\partial v_r^{(w)}}{\partial r} + \frac{\partial v_z^{(w)}}{\partial z}\right). \tag{D5}$$

In Equations D1–D5, p_f is the pore pressure, τ_{ij} is the total stress tensor, $v_i^{(u)}$ is the solid particle velocity, and $v_i^{(w)}$ is the relative fluid particle velocity. The corresponding equations of motion are given by:

$$\frac{\partial \tau_{rr}}{\partial r} + \frac{\partial \tau_{rz}}{\partial z} + \frac{\tau_{rr} - \tau_{\theta\theta}}{r} = \rho \dot{v}_r^{(u)} + \rho_f \dot{v}_r^{(w)}, \tag{D6}$$

$$\frac{\partial \tau_{zz}}{\partial z} + \frac{\partial \tau_{rz}}{\partial r} + \frac{\tau_{rz}}{r} = \rho \dot{v}_z^{(u)} + \rho_f \dot{v}_z^{(w)}, \tag{D7}$$

$$D_1 \dot{v}_r^{(w)} + D_2 v_r^{(w)} + \rho_f \dot{v}_r^{(u)} = -\frac{\partial p_f}{\partial r}, \tag{D8}$$

$$D_1 \dot{v}_z^{(w)} + D_2 v_z^{(w)} + \rho_f \dot{v}_z^{(u)} = -\frac{\partial p_f}{\partial z}. \tag{D9}$$

Equations D8 and D9 incorporate the low-frequency approximation to dynamic permeability (Masson et al., 2006), wherein the frequency-dependent permeability function is expanded in a Taylor series. This approximation captures the diffusive behavior of the slow wave at frequencies below the Biot characteristic frequency and enables a stable and computationally efficient implementation of Biot's equations in the FD scheme.

The poroelastic parameters in Equations D1–D9 are:

$$H = K_m + \frac{4}{3}\mu + M\alpha^2, \tag{D10}$$

$$C = M\alpha, \tag{D11}$$

$$M = \left(\frac{\alpha - \phi}{K_s} + \frac{\phi}{K_f}\right)^{-1}, \tag{D12}$$

$$\alpha = 1 - \frac{K_m}{K_s}, \tag{D13}$$

$$D_1 = \left(1 + \frac{2}{n_J}\right)\frac{\alpha_\infty \rho_f}{\phi}, \tag{D14}$$

$$D_2 = \frac{\eta}{\kappa_0}. \tag{D15}$$

Here, H, C, and M are the porous formation moduli; K_m and K_s are the frame and grain bulk moduli, respectively; μ is the shear modulus; α is the Biot-Willis constant; ϕ is porosity; K_f is the fluid bulk modulus; ρ_f is the fluid density. The parameter α_∞ represents the high-frequency tortuosity (Johnson et al., 1987), and η is the dynamic viscosity of the pore fluid. The dimensionless parameter n_J reflects microstructural properties of the porous medium–specifically, a weighted pore volume to grain surface ratio, the electrical formation factor, and the permeability (Masson et al., 2006). For clean sands, $n_J = 8$ is commonly assumed (Guan & Hu, 2011; Masson et al., 2006).

Our FD implementation is based on the method developed by Guan and Hu (2011) and extended by Ou and Wang (2019), in which the domain is divided into three sub-regions: acoustic (borehole), elastic, and poroelastic. A unified set of poroelastic equations is solved throughout the domain using limiting values of poroelastic parameters in the acoustic and elastic regions. Furthermore, additional boundary conditions are considered at the acoustic-poroelastic interface (open-pore condition) and the elastic-poroelastic interface (closed-pore condition), see Guan and Hu (2011) and Ou and Wang (2019) for more details. Non-splitting perfectly matched layers (NPML) are implemented at model boundaries, and the symmetry condition at $r = 0$ is enforced using a formulation derived via l'Hôpital's rule (Mittet & Renlie, 1996). Field quantities are assigned on a staggered grid following the layout described in Guan and Hu (2011). For initial conditions, we adopt an analytical solution for a normally incident plane P wave propagating in a homogeneous borehole environment (Peng, 1994). This initialization is consistent with the assumptions of our semi-analytical approach and facilitates direct comparison between the two approaches. Finally, we confirmed the accuracy of our FD implementation for elastic wave propagation by comparing with discrete-wavenumber integral (DWI) solutions from Tubman (1984) under typical acoustic logging conditions (source and receivers in the borehole).

Appendix E: Skempton Coefficient and Gassmann's Low-Frequency Limit for the Poroelastic Moduli

In the case of quasi-static, undrained condition where there is no fluid flux, one can derive the following relation from the stress-strain relation (Equation D1–D5):

$$\dot{p_f} = -C\left(\frac{v_r^{(u)}}{r} + \frac{\partial v_r^{(u)}}{\partial r} + \frac{\partial v_z^{(u)}}{\partial z}\right), \tag{E1}$$

$$\frac{1}{3}\dot{\tau}_{ii} = \left(H - \frac{4}{3}\mu\right)\left(\frac{v_r^{(u)}}{r} + \frac{\partial v_r^{(u)}}{\partial r} + \frac{\partial v_z^{(u)}}{\partial z}\right). \tag{E2}$$

It is then straightforward to derive the following relations:

$$p_f = -\frac{1}{3}B\tau_{ii}, \tag{E3}$$

$$B = \frac{M\alpha}{K_m + M\alpha^2}, \tag{E4}$$

where τ_{ii} indicates the trace of the total stress tensor in the poroelastic formation. We assume $p_f = 0$ at $t = 0$. The coefficient B is known as the Skempton coefficient (Rice & Cleary, 1976).

At the low-frequency limit where the relative fluid velocity is negligible, the undrained bulk modulus K_u is identified by the Gassmann equation:

$$K_u = K_m + M\alpha^2. \tag{E5}$$

Consequently, when the semi-analytical modeling approach (Section 2) is applied to the medium defined by the poroelastic properties, then K, E and ρ are calculated as,

$$K = K_u, \tag{E6}$$

$$E = \frac{9K_u\mu}{3K_u + \mu}, \tag{E7}$$

$$\rho = (1 - \phi)\rho_s + \phi\rho_f. \tag{E8}$$

Corresponding seismic velocities (V_P, V_S) are derived from K, E, and ρ above.

Appendix F: Effective-Source Formulation of the Generated Tube Waves Due To a Thin Porous Layer

Tube waves generated at the zone of a permeable structure were investigated in the past (Li et al., 1994). In this appendix, we reformulate the existing tube-wave generation model (Li et al., 1994) using the expressions that are consistent with the recent literature on open-fracture models (e.g., Bakku et al., 2013; Ionov, 2007; Minato, Ghose, Tsuji, et al., 2017). This formulation includes: (a) defining the continuity equation for the fluid volume due to the dynamic change of the layer thickness along with the relation between the fluid flow and the pressure gradient (i.e., Darcy's law), (b) deriving the volume of fluid flowing from the permeable structure (open fracture or porous layer) into the borehole by solving the continuity equation with appropriate boundary conditions, and (c) relating the fluid volume with the pressure amplitudes at the borehole. For a comparison, we also derive the tube-wave amplitude based on the same formulation using the diffusion equation considered in this paper (Equation 5).

We start from the continuity equation and Darcy's law, that are considered in an earlier model (see Equations 7 and 11 in Li et al., 1994):

$$-\frac{\partial q(r,\omega)}{\partial r} - \frac{q(r,\omega)}{r} = -i\omega\Delta L(\omega) - i\omega\frac{L_0}{K_d}\bar{p}(r,\omega), \tag{F1}$$

$$q(r,\omega) = -L_0\frac{\kappa_0}{\eta}\frac{\partial\bar{p}}{\partial r}, \tag{F2}$$

where $\bar{p}$ indicates the pressure within a porous layer as considered in Li et al. (1994), K_d is the drained bulk modulus of the layer, L_0 is the static layer thickness, and ΔL is the dynamic change of the thickness from L_0 due to elastic wave propagation. The dynamic thickness change ΔL can be defined as the difference in the vertical displacement between the upper and the lower boundaries of the layer followed by the small-L_0 approximation (Li et al., 1994):

$$\Delta L(\omega) = -k_p^2 L_0 D_E, \tag{F3}$$

where we use our notation of the potential amplitude (D_E). Note that K_d in Equation F1 is a free parameter, and one may assign any value which is a function of ϕ (Li et al., 1994). In this Appendix, we assume Reuss average, that is, $K_d^{-1} \approx \phi K_f^{-1} + (1 - \phi)K_s^{-1}$, as also suggested in Li et al. (1994). Equation F1 is solved for $\bar{p}$ with the following boundary condition at the borehole intersection:

$$\bar{p}(r,\omega)|_{r=R} = \overline{p_t}(\omega), \tag{F4}$$

where $\overline{p_t}$ is the generated tube-wave amplitude that we are interested in. This boundary condition (Equation F4) is suggested by Ionov (2007) and Bakku et al. (2013). On the other hand, the original formulation in Li et al. (1994) considers a constant boundary-value independent of time (see equation 15 in Li et al., 1994). This condition is the same as in Beydoun et al. (1985), where the tube-wave amplitude is assumed to be small (see the assumption 4 in Beydoun et al., 1985). Such assumption is not necessary for the boundary condition of Equation F4. Note that the original boundary condition in Li et al. (1994) can be obtained if we assume $\bar{p}(R, \omega) = 0$ ($\omega \neq 0$). Next, using Equations F1, F2, and F4, the pressure $\bar{p}$ can be solved as

$$\bar{p}(r, \omega) = \left(\overline{p_t} - \frac{\Delta L}{L_0} K_d\right) \frac{K_0\left(\sqrt{-i\omega}\, r/\bar{a}\right)}{K_0\left(\sqrt{-i\omega}\, R/\bar{a}\right)} + \frac{\Delta L}{L_0} K_d, \tag{F5}$$

where

$$\bar{a}^2 = \frac{\kappa_0 K_d}{\eta}. \tag{F6}$$

The rate of the fluid volume $\left(\Delta \bar{V}\ \mathrm{m}^3/s\right)$ flowing from the porous layer to the borehole is defined as

$$\Delta \bar{V} = -2\pi R q|_{r=R}, \tag{F7}$$

and the fluid volume is related to the generated tube-wave amplitude (e.g., Bakku et al., 2013; Ionov, 2007) as

$$\overline{p_t} = \frac{\rho_f C_T}{2\pi R^2} \Delta \bar{V}. \tag{F8}$$

Finally, using Equations F2, F5, F7, and F8, the tube-wave amplitude can be obtained as

$$\overline{p_t} = \frac{\rho_f C_T \frac{L_0}{R} \frac{\kappa_0}{\eta} \frac{\sqrt{-i\omega}}{\bar{a}} K_1\left(\sqrt{-i\omega}\, r/\bar{a}\right)/K_0\left(\sqrt{-i\omega}\, R/\bar{a}\right)}{1 + \rho_f C_T \frac{L_0}{R} \frac{\kappa_0}{\eta} \frac{\sqrt{-i\omega}}{\bar{a}} K_1\left(\sqrt{-i\omega}\, r/\bar{a}\right)/K_0\left(\sqrt{-i\omega}\, R/\bar{a}\right)} \frac{K_d \Delta L}{L_0}. \tag{F9}$$

Equation F9 is the effective-source model of the tube-wave amplitude based on Li et al. (1994).

Similar to the derivation above, one can derive the effective-source model based on the approach developed in this study. This is achieved by considering $p = \widetilde{p_t}$ in Equation 8 and using Equations F2, F7, and F8:

$$\widetilde{p_t} = \frac{\rho_f C_T \frac{L_0}{R} \frac{\kappa_0}{\eta} \frac{\sqrt{-i\omega}}{a} K_1\left(\sqrt{-i\omega}\, r/a\right)/K_0\left(\sqrt{-i\omega}\, R/a\right)}{1 + \rho_f C_T \frac{L_0}{R} \frac{\kappa_0}{\eta} \frac{\sqrt{-i\omega}}{a} K_1\left(\sqrt{-i\omega}\, r/a\right)/K_0\left(\sqrt{-i\omega}\, R/a\right)} p_{\mathrm{por}}^{\mathrm{ext}}. \tag{F10}$$

The definition of $p_{\mathrm{por}}^{\mathrm{ext}}$ can be found in Equation 7.

Appendix G: Summary of the Physical Quantities and the Notations

Table G1 summarizes the key physical parameters and symbols used throughout this study. While some quantities (e.g., E, K) are derived from poroelastic parameters under low-frequency approximation, we include all relevant notations for completeness and ease of reference.

Table G1
Glossary of Material and Wavefield Parameters Used in This Study

Symbol	Definition	Unit
K_m	Frame bulk modulus	Pa
K_s	Grain (solid) bulk modulus	Pa
K_f	Fluid bulk modulus	Pa
μ	Shear modulus of frame	Pa
ρ_s	Density of solid grains	kg/m^3
ρ_f	Density of pore fluid	kg/m^3
ρ	Bulk density of formation	kg/m^3
ϕ	Porosity	[–]
κ_0	Static permeability	m^2
ν	Dynamic viscosity of fluid	Pa· s
α_∞	High-frequency tortuosity	[–]
B	Skempton coefficient	[–]
V_P	Compressional wave velocity	m/s
V_S	Shear wave velocity	m/s
E	Young's modulus of formation	Pa
K	Bulk modulus of formation	Pa
k	Tube-wave wavenumber	rad/m
k_p	P-wave wavenumber	rad/m
K_{eff}	Effective bulk modulus of borehole fluid	Pa
C_T	Tube-wave phase velocity	m/s

Conflict of Interest

The authors declare no conflicts of interest relevant to this study.

Data Availability Statement

The MATLAB scripts implementing the semi-analytical tube-wave model, along with example files that reproduce representative numerical results in this paper, are licensed under MIT and published on GitHub https://github.com/sminatos/tubewave-simulation-matlab (Minato, 2025b). The Julia scripts implementing finite-difference poroelastic modeling, together with example files that reproduce representative numerical results in this paper, are licensed under MIT and published on GitHub https://github.com/sminatos/FDModBiotCyl.jl (Minato, 2025a).

References

Aki, K., & Richards, P. G. (2002). Propagator matrix method. In J. Ellis (Ed.), *Quantitative seismology* (2nd ed., pp. 269–282). University Science Books.

Bakku, S. K., Fehler, M., & Burns, D. (2013). Fracture compliance estimation using borehole tube waves. *Geophysics*, *78*(4), D249–D260. https://doi.org/10.1190/GEO2012-0521.1

Bakulin, A., Sidorov, A., Kashtan, B., & Jaaskelainen, M. (2008). Real-time completion monitoring with acoustic waves. *Geophysics*, *73*(1), E15–E33. https://doi.org/10.1190/1.2818117

Bense, V., Gleeson, T., Loveless, S., Bour, O., & Scibek, J. (2013). Fault zone hydrogeology. *Earth-Science Reviews*, *127*, 171–192. https://doi.org/10.1016/j.earscirev.2013.09.008

Beydoun, W., Cheng, C., & Toksöz, M. (1985). Detection of open fractures with vertical seismic profiling. *Journal of Geophysical Research*, *90*(B6), 4557–4566. https://doi.org/10.1029/jb090ib06p04557

Biot, M. A. (1952). Propagation of elastic waves in a cylindrical bore containing a fluid. *Journal of Applied Physics*, *23*(9), 997–1005. https://doi.org/10.1063/1.1702365

Biot, M. A. (1956a). Theory of propagation of elastic waves in a fluid-saturated porous solid. II. Higher frequency range. *Journal of the Acoustical Society of America*, *28*(2), 179–191. https://doi.org/10.1121/1.1908241

Biot, M. A. (1956b). Theory of propagation of elastic waves in a fluid-saturated porous solid. I. Low-frequency range. *Journal of the Acoustical Society of America*, *28*(2), 168–178. https://doi.org/10.1121/1.1908239

Biot, M. A. (1962). Mechanics of deformation and acoustic propagation in porous media. *Journal of Applied Physics*, *33*(4), 1482–1498. https://doi.org/10.1063/1.1728759

Chang, S. K., Liu, H. L., & Johnson, D. L. (1988). Low-frequency tube waves in permeable rocks. *Geophysics*, *53*(4), 519–527. https://doi.org/10.1190/1.1442483

Cheng, C., Jinzhong, Z., & Burns, D. R. (1987). Effects of in situ permeability on the propagation of Stoneley (tube) waves in a borehole. *Geophysics*, *52*(9), 1279–1289. https://doi.org/10.1190/1.1442388

Cook, P. G. (2003). *A guide to regional groundwater flow in fractured rock aquifers*. Seaview Press.

Endo, T. (2006). Evaluation of formation permeability from borehole Stoneley waves. *Journal of Geography*, *115*(3), 383–399. https://doi.org/10.5026/jgeography.115.3_383

Evans, K. F., Genter, A., & Sausse, J. (2005). Permeability creation and damage due to massive fluid injections into granite at 3.5 km at Soultz: 1. Borehole observations. *Journal of Geophysical Research*, *110*(B4). https://doi.org/10.1029/2004jb003168

Fan, H., & Smeulders, D. (2013). Shock-induced wave propagation over porous and fractured borehole zones: Theory and experiments. *Journal of the Acoustical Society of America*, *134*(6), 4792–4800. https://doi.org/10.1121/1.4826950

Gebraad, L., Boehm, C., & Fichtner, A. (2020). Bayesian elastic full-waveform inversion using Hamiltonian Monte Carlo. *Journal of Geophysical Research: Solid Earth*, *125*(3), e2019JB018428. https://doi.org/10.1029/2019jb018428

Gilbert, F., & Backus, G. E. (1966). Propagator matrices in elastic wave and vibration problems. *Geophysics*, *31*(2), 326–332. https://doi.org/10.1190/1.1439771

Greenwood, A., Caspari, E., Egli, D., Baron, L., Zahner, T., Hunziker, J., & Holliger, K. (2019). Characterization and imaging of a hydrothermally active near-vertical fault zone in crystalline rocks based on hydrophone VSP data. *Tectonophysics*, *750*, 153–176. https://doi.org/10.1016/j.tecto.2018.11.015

Greenwood, A., Dupuis, C. J., Urosevic, M., & Kepic, A. (2012). Hydrophone VSP surveys in hard rock. *Geophysics*, *77*(5), WC223–WC234. https://doi.org/10.1190/geo2011-0490.1

Guan, W., & Hu, H. (2011). The parameter averaging technique in finite-difference modeling of elastic waves in combined structures with solid, fluid and porous subregions. *Communications in Computational Physics*, *10*(3), 695–715. https://doi.org/10.4208/cicp.020810.161210a

Hardage, B. (1981). An examination of tube wave noise in vertical seismic profiling data. *Geophysics*, *46*(6), 892–903. https://doi.org/10.1190/1.1441228

Hardin, E., Cheng, C., Paillet, F., & Mendelson, J. (1987). Fracture characterization by means of attenuation and generation of tube waves in fractured crystalline rock at Mirror Lake, New Hampshire. *Journal of Geophysical Research*, *92*(B8), 7989–8006. https://doi.org/10.1029/JB092iB08p07989

Huang, C., & Hunter, J. (1984). The tube-wave method of estimating in-situ rock fracture permeability in fluid-filled boreholes. *Geoexploration*, *22*(3–4), 245–259. https://doi.org/10.1016/0016-7142(84)90015-2

Hunziker, J., Greenwood, A., Minato, S., Barbosa, N. D., Caspari, E., & Holliger, K. (2020). Bayesian full-waveform inversion of tube waves to estimate fracture aperture and compliance. *Solid Earth*, *11*(2), 657–668. https://doi.org/10.5194/se-11-657-2020

Ionov, A. M. (2007). Stoneley wave generation by an incident P-wave propagating in the surrounding formation across a horizontal fluid-filled fracture. *Geophysical Prospecting*, *55*(1), 71–82. https://doi.org/10.1111/j.1365-2478.2006.00577.x

Ionov, A. M., & Maximov, G. A. (1996). Propagation of tube waves generated by an external source in layered permeable rocks. *Geophysical Journal International*, *124*(3), 888–906. https://doi.org/10.1111/j.1365-246X.1996.tb05643.x

Johnson, D. L., Koplik, J., & Dashen, R. (1987). Theory of dynamic permeability and tortuosity in fluid-saturated porous media. *Journal of Fluid Mechanics*, *176*, 379–402. https://doi.org/10.1017/s0022112087000727

Kiguchi, T., Ito, H., Kuwahara, Y., & Miyazaki, T. (2001). Estimating the permeability of the Nojima Fault Zone by a hydrophone vertical seismic profiling experiment. *Island Arc*, *10*(3–4), 348–356. https://doi.org/10.1111/j.1440-1738.2001.00333.x

Kurkjian, A., Coates, R., White, J., & Schmidt, H. (1994). Finite-difference and frequency-wavenumber modeling of seismic monopole sources and receivers in fluid-filled boreholes. *Geophysics*, *59*(7), 1053–1064. https://doi.org/10.1190/1.1443661

Li, Y., Rabbel, W., & Wang, R. (1994). Investigation of permeable fracture zones by tube-wave analysis. *Geophysical Journal International*, *116*(3), 739–753. https://doi.org/10.1111/j.1365-246x.1994.tb03294.x

Marzetta, T. L., Orton, M., Krampe, A., Johnston, L. K., & Wuenschel, P. C. (1988). A hydrophone vertical seismic profiling experiment. *Geophysics*, *53*(11), 1437–1444. https://doi.org/10.1190/1.1442423

Masson, Y. J., Pride, S. R., & Nihei, K. T. (2006). Finite difference modeling of Biot's poroelastic equations at seismic frequencies. *Journal of Geophysical Research*, *111*(B10). https://doi.org/10.1029/2006JB004366

Milligan, P. A., Rector III, J. W., & Bainer, R. W. (1997). Hydrophone VSP imaging at a shallow site. *Geophysics*, *62*(3), 842–852. https://doi.org/10.1190/1.1444193

Minato, S. (2025a). sminatos/FDModBiotCyl.jl: Version 1.0.1 [Software]. *Zenodo*. https://doi.org/10.5281/zenodo.17481901

Minato, S. (2025b). sminatos/tubewave-simulation-matlab: Version 1.0.1 [Software]. *Zenodo*. https://doi.org/10.5281/zenodo.17481934

Minato, S., & Ghose, R. (2017). Low-frequency guided waves in a fluid-filled borehole: Simultaneous effects of generation and scattering due to multiple fractures. *Journal of Applied Physics*, *121*(10), 104902. https://doi.org/10.1063/1.4978250

Minato, S., Ghose, R., Kiguchi, T., & Tsuji, T. (2017). Characterization of hydraulic properties of a dipping permeable layer using the amplitude of the generated tube wave. In *SEG technical program expanded abstracts 2017* (pp. 953–958). Society of Exploration Geophysicists.

Minato, S., Ghose, R., Tsuji, T., Ikeda, M., & Onishi, K. (2017). Hydraulic properties of closely spaced dipping open fractures intersecting a fluid-filled borehole derived from tube wave generation and scattering. *Journal of Geophysical Research: Solid Earth*, *122*(10), 8003–8020. https://doi.org/10.1002/2017JB014681

Mittet, R., & Renlie, L. (1996). High-order, finite-difference modeling of multipole logging in formations with anisotropic attenuation and elasticity. *Geophysics*, *61*(1), 21–33. https://doi.org/10.1190/1.1443942

Ou, W., & Wang, Z. (2019). Simulation of Stoneley wave reflection from porous formation in borehole using FDTD method. *Geophysical Journal International*, *217*(3), 2081–2096. https://doi.org/10.1093/gji/ggz144

Peng, C. (1994). *Borehole effects on downhole seismic measurements*. (Ph.D. thesis, Massachusetts Institute of Technology). Retrieved from http://hdl.handle.net/1721.1/12218

Peng, C., Lee, J. M., & Toksöz, M. N. (1996). Pressure in a fluid-filled borehole caused by a seismic source in stratified media. *Geophysics*, *61*(1), 43–55. https://doi.org/10.1190/1.1443955

Peng, C., & Toksoz, N. (1992). Tube wave generation at a layer boundary for an incident compressional plane wave. In *Earth resources laboratory industry consortia annual report;1992-14 (Technical report)* (pp. 337–370). Massachusetts Institute of Technology. Retrieved from http://hdl.handle.net/1721.1/75197

Randall, C. (1991). Multipole acoustic waveforms in nonaxisymmetric boreholes and formations. *Journal of the Acoustical Society of America*, *90*(3), 1620–1631. https://doi.org/10.1121/1.401903

Rice, J. R., & Cleary, M. P. (1976). Some basic stress diffusion solutions for fluid-saturated elastic porous media with compressible constituents. *Reviews of Geophysics*, *14*(2), 227–241. https://doi.org/10.1029/rg014i002p00227

Schoenberg, M. (1986). Fluid and solid motion in the neighborhood of a fluid-filled borehole due to the passage of a low-frequency elastic plane wave. *Geophysics*, *51*(6), 1191–1205. https://doi.org/10.1190/1.1442174

Sidler, R., Carcione, J. M., & Holliger, K. (2014). A pseudospectral method for the simulation of 3-D ultrasonic and seismic waves in heterogeneous poroelastic borehole environments. *Geophysical Journal International*, *196*(2), 1134–1151. https://doi.org/10.1093/gji/ggt447

Sinha, B. K., & Asvadurov, S. (2004). Dispersion and radial depth of investigation of borehole modes. *Geophysical Prospecting*, *52*(4), 271–286. https://doi.org/10.1111/j.1365-2478.2004.00415.x

Tang, X. M., & Cheng, C. H. (1993). Borehole Stoneley wave propagation across permeable structures. *Geophysical Prospecting*, *41*(2), 165–187. https://doi.org/10.1111/j.1365-2478.1993.tb00864.x

Tang, X. M., & Cheng, C. H. (1996). Fast inversion of formation permeability from Stoneley wave logs using a simplified Biot-Rosenbaum model. *Geophysics*, *61*(3), 639–645. https://doi.org/10.1190/1.1443993

Tang, X. M., Cheng, C. H., & Toksöz, M. N. (1991). Dynamic permeability and borehole Stoneley waves: A simplified Biot–Rosenbaum model. *Journal of the Acoustical Society of America*, *90*(3), 1632–1646. https://doi.org/10.1121/1.401904

Tezuka, K., Cheng, C. H. A., & Tang, X. M. (1997). Modeling of low-frequency Stoneley-wave propagation in an irregular borehole. *Geophysics*, *62*(4), 1047–1058. https://doi.org/10.1190/1.1444206

Tubman, K. M. (1984). *Full waveform acoustic logs in radially layered boreholes*. (Ph.D. thesis, Massachusetts Institute of Technology). Retrieved from http://hdl.handle.net/1721.1/15358

Uehara, S., & Shimamoto, T. (2004). Gas permeability evolution of cataclasite and fault gouge in triaxial compression and implications for changes in fault-zone permeability structure through the earthquake cycle. *Tectonophysics*, *378*(3–4), 183–195. https://doi.org/10.1016/j.tecto.2003.09.007

White, J. E. (1953). Signals in a borehole due to plane waves in the solid. *Journal of the Acoustical Society of America*, *25*(5), 906–915. https://doi.org/10.1121/1.1907217

White, J. E. (1983). *Underground sound: Application of seismic waves* (Vol. 253). Elsevier.

White, J. E., & Lessenger, M. A. (1988). Caliper effect on borehole coupling. *Exploration Geophysics*, *19*(2), 201–205. https://doi.org/10.1071/eg988201

Wibberley, C. A., Yielding, G., & Di Toro, G. (2008). Recent advances in the understanding of fault zone internal structure: A review. *Geological Society, London, Special Publications*, *299*(1), 5–33. https://doi.org/10.1144/sp299.2